T cell-instructed inflammation drives immune checkpoint inhibitor therapy resistance.

Nam Woo Cho[1,2], Sophia M. Guldberg[2,3], Eun Ji Kim[4], Kamir J. Hiam-Galvez[2,3], Katherine Wai[2], Lauren S. Levine[2,5], Barzin Y. Nabet[6], Rachel DeBarge[2,3], Jacqueline L. Yee[2,3], Naa Asheley Ashitey[2], Iliana Tenvooren[2], Matthew H. Spitzer[2,3]

[1]Department of Radiation Oncology, University of California, San Francisco, San Francisco, CA, USA

[2]Departments of Otolaryngology and Microbiology & Immunology, Helen Diller Family Comprehensive Cancer Center, Parker Institute for Cancer Immunotherapy, Chan Zuckerberg Biohub, University of California, San Francisco, San Francisco, CA, USA

[3]Graduate Program in Biomedical Sciences, University of California, San Francisco, San Francisco, CA, USA

[4]Independent researcher

[5]Department of Medicine, University of California, San Francisco, San Francisco, CA, USA

[6]Genentech, South San Francisco, CA, USA

Abstract

Even in patients whose tumours exhibit increased T cell infiltration, resistance to immune checkpoint inhibitor (ICI) therapy is common. We investigated mechanisms of ICI resistance using engineered mouse models with increased neoantigen burden and T cell infiltration. We found that in ICI-resistant tumours, T cells upregulate an NF-κB-driven inflammatory circuit in the tumour microenvironment (TME), culminating in PMN-MDSC recruitment and tumour escape. This resistance circuit was molecularly driven by IL-1, TNFα, and G-CSF, and their genetic or pharmacologic inhibition increased ICI efficacy. Furthermore, we identified a subset of human *TNF*-expressing T cells that expand following ICI therapy and are associated with increased tumour NF-κB signaling. These data reveal a surprising mechanism of ICI resistance whereby T cells instruct NF-κB-mediated inflammation to paradoxically drive a resistance circuit in participating tumours, refining our understanding of ICI response and resistance with important therapeutic implications.

27 **Main**

28 Immune checkpoint inhibitors (ICIs) are integral to our armamentarium against cancer. However, these
29 therapies are not effective in many patients, and an important mission is to better define fundamental immunologic
30 principles determining treatment response versus failure[1]. Among core immunologic programs governing the
31 response to ICIs is the infiltration of T cells in the tumour microenvironment (TME)[2–5], where "inflamed" or "hot"
32 tumours, such as those with microsatellite instability-high (MSI-H) status, exhibit higher response rates to further
33 immune activating therapies[6–10].

34 While often referred to as "inflamed" tumours, "inflammation" is a broad term encompassing multiple
35 processes that can promote or prevent tumour progression[11]. For instance, inflammation can be driven by the
36 transcription factor nuclear factor-κB (NF-κB), which is activated in multiple cell types in the TME by various
37 stimuli, including the cytokines TNFα and IL-1[12,13]. This circuit can drive diverse tumour promoting mechanisms
38 including immunosuppression[14–18], and accordingly, its inhibition in the TME can lead to improved immunologic
39 control of tumours[19–24].

40 Of note, these two components that can each define inflammation in the TME – T cells and NF-κB-
41 mediated inflammation – can co-exist in the TME, yet their relationship is incompletely defined. much of the
42 recent research efforts have focused on the biology of tumour infiltrating lymphocytes (TILs) at the end of the
43 immune response cascade against cancer, with loss of stemness and differentiation toward exhaustion[25.] Among
44 many known roles, NF-κB signaling can foster myeloid-derived suppressor cell (MDSC) recruitment and
45 activation to suppress T cell cytotoxicity[20,26–29]. However, it is currently unknown is whether conventional CD4
46 or CD8 T cells themselves regulate NF-κB-mediated inflammation in the TME, helping to shape the immunologic
47 setpoint and thus modulate responsiveness to immunotherapy.

48 Here, we use new mouse syngeneic tumour models of ICI response and resistance to discover that T cells
49 can instruct an NF-κB inflammatory circuit in the TME, driving ICI resistance. We found that ICI-resistant
50 tumours escape immune control by upregulation of IL-1-driven, NF-κB-transcribed cytokines including G-CSF
51 and CXCL1, which subsequently recruit polymorphonuclear myeloid-derived suppressor cells (PMN-MDSCs).
52 Importantly, we show that this inflammatory resistance circuit requires T cells. Furthermore, we found that

53 stimulated tumour-infiltrating CD8 T cells are sufficient to drive G-CSF production by tumour cells *in vitro* in a
54 TNFα-dependent manner. *In vivo,* ICIs increase infiltration of TNFα-producing T cells and neutrophils. Breaking
55 this NF-κB inflammatory circuit via elimination of IL-1 or G-CSF signaling, or especially by host-derived TNFα,
56 sensitized the resistant tumours to ICIs. Finally, analyses of human datasets corroborate these cellular and
57 mechanistic elements in patients with breast cancer or MSI-H tumours treated with ICIs. These findings refine
58 the current paradigm of T cell responses to ICI therapy with significant clinical implications, revealing an
59 opportunity to dissociate the tumour-promoting aspects of T cell activity from their tumouricidal functions to
60 improve therapeutic benefit.
61
62 **Results**
63 Mouse MSI-H syngeneic tumours demonstrate variable responses to ICIs
64 To understand T cell-dependent mechanisms of ICI response and resistance, we sought to exclude mutated
65 cancer antigen (neoantigen) availability as a limiting factor[1]. To this end, we generated mouse syngeneic tumour
66 cell lines with increased neoantigen load by knocking out the DNA mismatch repair protein, MSH2, to create
67 mismatch repair deficiency (MMRd). MMRd tumours develop MSI over time, which often increases tumour
68 neoantigen load and T cell infiltration[9,10,30–33]. While the response rates to ICIs are generally favorable, treatment
69 failure is frequently seen in mouse and human[7,32,34]. This presents an opportunity to study ICI response and
70 resistance in the context of T cell inflammation. *Msh2* gene deletion by CRISPR-Cas9 ribonucleoprotein
71 electroporation[35] in the polyclonal cell pool almost completely abolished MSH2 protein expression, eliminating
72 the requirement for single cell cloning and allowing preservation of any parental tumour heterogeneity (Fig. 1a,
73 Extended Data Fig. 1a). All four cell lines generated in this manner – B16F10 melanoma, AT3 breast, EO771
74 breast, and 4T1 breast – accumulated microsatellite instability over 4 months, or 60 passages, of continuous
75 culture when assessed by PCR[9,36] (Fig. 1b, Extended Data Fig. 1b). Compared to control microsatellite-stable
76 (MSS) cell lines generated using nontargeting CRISPR-Cas9 guide RNA and cultured for the same duration,
77 B16F10 MSI-H and AT3 MSI-H cell lines accumulated single nucleotide polymorphisms and indels when

78 quantified by whole exome sequencing (Fig. 1c). These data are consistent with the level of MSI reported in
79 published mouse studies[9,10].

80 Notably, when implanted into syngeneic wild type mice, the panel of tumours demonstrated variability in
81 their responsiveness or resistance to combination ICI treatment of anti-PD-1 and anti-CTLA4. The B16F10 MSI-
82 H subcutaneous tumours exhibited improved response to ICIs compared to control (Fig. 1d). Additionally, ICIs
83 led to rejection of EO771 MSI-H tumours (Extended Data Fig. 1c). However, the AT3 MSI-H and 4T1 MSI-H
84 orthotopic breast tumours did not respond to ICIs (Fig. 1e, Extended Data Fig. 1d). Thus, the ICI response rates
85 across our panel of tumour models mirror the observed rates for human MSI-H cancers[32,37]. In the AT3 model,
86 ICI resistance was not attributable to faster growth of MSI-H cells or decreased MHC-I expression (Extended
87 Data Fig. 1e,f). Compared to B16F10 MSI-H cells, AT3 MSI-H cells accumulated more than twice the number
88 of SNPs and indels (Fig. 1c). AT3 MSI-H cells also transcribed neoantigens with similar predicted antigenicity
89 and allele frequency as B16F10 MSI-H cells, calculated using MuPeXI with inputs including neopeptide
90 sequences, predicted MHC binding affinities and gene expression[38] (Fig. 1f,g).

91

92 <u>CD8 T cells increase in both ICI responsive and resistant tumours but assume distinct phenotypic states</u>

93 We next used mass cytometry by time-of-flight (CyTOF) to explore immunologic mechanisms that could
94 explain the divergent responses to ICIs in our mouse models. An analysis of major immune cell types in the TME
95 revealed that ICI-treated AT3 MSI-H tumours do accumulate more CD8 T cells compared to IgG-treated tumours
96 or AT3 MSS tumours, similar to ICI-treated B16F10 MSI-H tumours (Fig. 2a,b, Extended Data Fig. 2a). In each
97 model, principal component analysis of immune cell subset frequencies demonstrated that the principal
98 component spaces occupied by ICI-treated MSI-H tumours are in part driven by increases in CD8 T cell subsets
99 (Extended Data Fig. 2b,c). Thus, the ICI resistance in the AT3 MSI-H model is unlikely to be attributable to
100 insufficient numbers of tumour infiltrating lymphocytes (TILs).

101 To further explore phenotypic differences in AT3 vs. B16F10 TILs under each condition, we sampled
102 CD8 T cells and performed Uniform Manifold Approximation and Projection (UMAP)[39], Phenograph[40], and
103 Slingshot pseudotime trajectory analyses[41]. This revealed three pseudotime lineages outlining the relationship

104 between 9 total clusters identified by Phenograph, starting from cluster 9 comprising naïve CD8 T cells that are
105 CD44- and CD62L+ (Fig 2c,d, Extended Data Fig. 2d). With ICIs, the majority of CD8 T cells in MSI-H tumours
106 of either model occupied clusters belonging to lineage 1, comprising Ly6C+ T cells (Fig. 2e,f). Notably, CD8 T
107 cells in B16F10 MSI-H tumours treated with ICIs were most enriched in clusters 2 and 3 toward the end of lineage
108 1, whereas in AT3 MSI-H ICI treated tumours they were enriched in clusters 4 and 6 in earlier pseudotime (Fig.
109 2e,f, Extended Data Fig. 2e). Cells in clusters 2 and 3 expressed higher amounts of markers of proliferating
110 cytotoxic effector CD8 T cells with evidence of increasing exhaustion (PD-1, Tim3, CD39) and effector function
111 (Ki-67, Granzyme B (GrB)) along pseudotime. In comparison, CD8 T cells in clusters 4 and 6 expressed lower
112 amounts of each of these markers except for CD69, which was highly expressed (Fig. 2g). This suggests
113 predominance of transitional and terminally exhausted CD8 T cells in the B16F10 model with ICIs, while AT3
114 MSI-H tumours contain cells of an early activated phenotype[42] with lower cytotoxic potential compared to
115 B16F10 infiltrating cells. Quantification of manually gated Ki-67+ GrB+ CD8 T cells confirmed increased
116 infiltration into ICI-treated B16F10 MSI-H tumours compared to IgG control, whereas this population was more
117 sparse and did not increase with ICIs in AT3 MSI-H tumours (Fig. 2h,i). Similarly, analysis of effector/effector
118 memory (CD44+ CD62L-) CD8 T cells in peripheral blood and spleen demonstrated reduced expression of GrB
119 and Ki-67 in AT3 tumour-bearing mice (Fig. 2j). Finally, assessment of CD4 T cells in each model showed
120 minimal expansion of conventional CD4 T cells in ICI-treated AT3 MSI-H tumours compared to IgG controls or
121 MSS tumours, with a similarly minimal increase in Ki-67 and PD-1 (Extended Data Fig. 2f,g). In sum, these data
122 show that, despite increased T cell infiltrates in MSI-H tumours, T cells in the responsive B16F10 and resistant
123 AT3 models assume distinct phenotypic states that are consistent with the divergent ICI responses.
124
125 <u>An NF-κB-mediated inflammatory program drives immunosuppression in the ICI-resistant TME</u>
126 Next, we focused on determining cell types and pathways that contribute to the divergent phenotypic states
127 of T cells in each model. AT3 MSI-H tumours treated with ICIs were infiltrated with significantly more
128 neutrophils compared to IgG-treated controls or B16F10 MSI-H tumours with or without treatment (Fig. 3a).
129 Sorted neutrophils from ICI-treated AT3 MSI-H tumours suppressed OT-I T cell proliferation *in vitro* (Extended

130 Data Fig. 3a), consistent with function of polymorphonuclear myeloid-derived suppressor cells (PMN-MDSCs)
131 that are extensively described in the context of cancer[43]. Compared to mice with B16F10 MSI-H tumours, those
132 with AT3 MSI-H tumours exhibited significantly more correlations between neutrophil cell subsets and other
133 immune cell subsets throughout the system, across tumour, blood, tumour-draining lymph node and spleen (Fig.
134 3b), suggesting system-wide coordination similar to what we have recently described for the parental AT3 model[44].
135 Thus, we next examined the cytokine milieu of the TME and peripheral blood to understand factors that can drive
136 these changes in the AT3 MSI-H tumour bearing mice. Principal component analysis of cytokines in tumour
137 lysate or plasma revealed that ICI treatment resulted in increased levels of cytokines/chemokines regulated by the
138 NF-κB pathway (TNFα, IL-1α, G-CSF, CXCL1, CXCL2, IL-6) (Fig. 3c,d). Indeed, further quantification in
139 tumour lysates confirmed that ICI treatment results in increased amounts of the neutrophil growth factor G-CSF,
140 and neutrophil chemoattractants CXCL1 (Fig. 3e) and CXCL2 (Extended Data Fig. 3b). Quantitative PCR of *Csf3*
141 (coding for G-CSF) and *Cxcl1* transcripts from sorted cells from the TME showed that tumour cells increase
142 expression of both transcripts upon ICI treatment (Fig. 3f, Extended Data Fig. 3c). These data are consistent with
143 our own data and the literature reporting production of G-CSF and CXCL1 from mouse and human tumours[44–48]
144 and suggest that ICI treatment further drives upregulation of this existing circuit.

145 Furthermore, we recently reported that G-CSF production by AT3 tumour cells is dependent on signaling
146 through the IL-1 receptor (IL-1R)[44]. Of note, IL-1α and IL-1β are both known to synergize with TNFα through
147 the canonical NF-κB pathway to upregulate G-CSF, CXCL1 and CXCL2 production[49]. We confirmed that AT3
148 MSS and MSI-H cells increase G-CSF production after TNFα and IL-1α stimulation *in vitro,* in contrast to
149 B16F10 MSS and MSI-H tumour cells (Fig. 3g, Extended Data Fig. 3d). In accordance with these observations,
150 treatment of cells *in vitro* resulted in a significantly greater degradation of IκBα in AT3 MSI-H cells compared
151 to B16F10 MSI-H cells, consistent with greater capacity for NF-κB pathway activation in the AT3 model (Fig.
152 3h). *In vivo,* blockade of IL-1 signaling with IL-1R neutralizing antibody reduced G-CSF and CXCL1 in AT3
153 MSI-H tumours and synergized with ICIs to improve tumour control (Fig. 3i,j, Extended Data Fig. 3e).
154 Additionally, elimination of host G-CSF receptor signaling in *Csf3r* knock-out mice improved ICI efficacy against
155 AT3 MSI-H tumours (Fig. 3k, Extended Data Fig. 3f).

156 We then went on to examine the relevance of this mechanism in a mouse model that exhibits more variable
157 responses to ICIs - the MOC1 syngeneic model of head and neck squamous cell carcinoma. In this model, only a
158 fraction of mice exhibits responses to ICIs (Extended Data Fig. 3g). We confirmed that these subcutaneous MOC1
159 tumours exhibit the key molecular features of the inflammation-mediated resistance circuit, including production
160 of IL-1α and G-CSF (Extended Data Fig. 3h). We also examined the abundance and activation of immune cells
161 in the TME after ICI treatment and associated these changes with tumour growth across individual mice.
162 Consistent with our hypothesis, we found that animals resistant to ICIs exhibited significantly higher plasma G-
163 CSF levels and more neutrophils in the TME and spleen early after treatment compared to responders (Extended
164 Data Fig. 3i,j). In sum, these data collectively show that ICI resistance in these mouse models can be mediated
165 by upregulation of classical NF-κB signaling target genes through a circuit that recruits T cell-suppressive PMN-
166 MDSCs to the TME.
167
168 <u>T cells drive activation of the inflammatory ICI resistance circuit</u>
169 Because this inflammatory circuit was intensified in ICI-treated AT3 MSI-H tumours with increased CD8
170 T cell infiltration, we hypothesized that T cells may paradoxically exacerbate the inflammatory resistance
171 program when infiltrating into a TME with an active NF-κB inflammatory circuit. Indeed, neutrophils were only
172 increased in the TME of late passage MSI-H AT3 tumours and not in tumours that had just undergone MSH2
173 knockout and have not yet accumulated MSI mutations (Fig. 4a), suggesting that perhaps T cells responding to
174 increased tumour neoantigens may activate the inflammatory circuit. Depleting T cells in AT3 MSI-H tumours
175 using an anti-Thy1 antibody strikingly decreased G-CSF and CXCL1 protein levels as well as neutrophil
176 infiltration in the TME (Fig. 4b-d). Using anti-CD4 and anti-CD8 antibodies for T cell depletion phenocopied
177 reduction in G-CSF and CXCL1, requiring elimination of both cell types (Extended Data Fig. 4a). Moreover, co-
178 culturing CD3/CD28-stimulated CD8 T cells sorted from AT3 MSI-H tumours together with AT3 MSI-H tumour
179 cells increased G-CSF production as quantified in the supernatant by more than five-fold, indicating that CD8 T
180 cells can be sufficient to drive this circuit (Fig. 4e).

181 Of the canonical cytokines produced by activated CD8 T cells, TNFα signals through the NF-κB pathway.
182 Importantly, the increase in G-CSF was largely dependent on TNFα, as the addition of a neutralizing antibody to
183 TNFα resulted in a significant reduction of G-CSF (Fig. 4e). Neutralization of other potential T cell factors, such
184 as FasL or GM-CSF, did not result in reduction of G-CSF (Extended Data Fig. 4b). We thus hypothesized that
185 TNFα-expressing T cells could drive the NF-κB inflammatory resistance circuit. Quantification of TNFα+ CD4
186 and CD8 T cells in AT3 MSI-H tumour and spleen revealed that ICIs increase each subset specifically in the TME
187 (Fig. 4f). This was also accompanied by increases in TNFα+ tumour infiltrating neutrophils, a cell type well-
188 known to express TNFα[50] (Extended Data Fig. 4c). Finally, we implanted AT3 MSI-H tumours in *Tnf* knockout
189 mice lacking host-derived TNFα, which resulted in tumour rejection upon ICI treatment (Fig. 4g, Extended Data
190 Fig. 4d). Treatment with etanercept, a TNFα-binding inhibitor[51], also enhanced ICI efficacy in these tumours (Fig.
191 4h, Extended Data Fig. 4e). Collectively, these data support a novel mechanism whereby ICI treatment induces
192 T cell infiltration and activation that can drive a TNFα- and IL-1-dependent, tumour-promoting inflammation
193 circuit. This exacerbates an immunosuppressive TME and results in treatment resistance, even in the context of
194 highly-mutated tumours.
195
196 ICI treatment induces *TNF*+ CD8 T cells associated with increased tumour NF-κB signaling in breast cancer
197 We next sought to interrogate our model of T cell-induced NF-κB tumour inflammation in human cancer.
198 To this end, we analyzed a publicly available single-cell RNA sequencing dataset of tumour samples from non-
199 metastatic breast cancer patients before and after a single dose of pembrolizumab[52]. A total of 7 clusters were
200 identified across all CD8 T cells (Fig. 5a and Extended Data Fig. 5a). Notably, we observed a separation of
201 *GZMB*-expressing CD8 T cells and those that express *TNF* (Fig. 5b). While the density of *GZMB*-expressing cells
202 was highest in the *GZMB*+ Exhausted cluster, the density of cells expressing *TNF* was highest in a distinct cluster
203 characterized by cells co-expressing *TNF* as well as high levels of *GZMK*, coding for Granzyme K (GrK) (*TNF*+
204 *GZMK*+ cluster) (Fig. 5b and Extended Data Fig. 5b). Comparison of differentially expressed genes across the
205 two clusters revealed higher expression of markers of cytotoxicity and exhaustion in the *GZMB*+ Exhausted
206 cluster (*GZMB, CXCL13, IFNG, PDCD1, CTLA4, LAG3, HAVCR2,* and *TOX*), most resembling the mouse CD8

207 T cell clusters 2 and 3 that are enriched in ICI-treated B16F10 MSI-H tumours (Fig. 2c-i). In contrast, cells in the
208 *TNF*+ *GZMK*+ cluster displayed higher expression of markers suggestive of early activation (*CD69, FOS, DUSP1,*
209 *RPL13*) and absence of exhaustion markers (Fig. 5c), resembling the mouse CD8 T cell clusters 4 and 6 that are
210 enriched in ICI-treated AT3 MSI-H tumours (Fig. 2c-i). Additionally, a smaller group of *TNF*- and *IFNG*-
211 expressing cells (*TNF*+ *IFNG*+ Exhausted) was identified, which were transcriptionally similar to cells in the
212 *GZMB*+ Exhausted cluster (Fig. 5a and Extended Data Fig. 5a,c,d). Given the parallel between cells in the *GZMB*+
213 Exhausted cluster and the *TNF*+ *GZMK*+ cluster compared to cells in the ICI responsive B16F10 and resistant
214 AT3 tumours respectively, we further examined the behavior of these clusters. In aggregate, we found that the
215 *TNF*+ *GZMK*+ cluster was more frequent post-pembrolizumab on-treatment ("On"), compared to pre-
216 pembrolizumab ("Pre") (Fig. 5d). When analyzed per-patient, the *TNF*+ *GZMK*+ cluster significantly increased
217 following pembrolizumab, whereas the *GZMB*+ Exhausted cluster only increased in a subset of patients (Fig. 5e,
218 Extended Data Fig. 5e). These data suggested that a subset of *TNF*-expressing CD8 T cells characterized by lack
219 of a cytotoxicity and exhaustion signature can expand following ICI therapy. Informed by our results in mouse
220 models, we hypothesized that these cells may stimulate NF-κB inflammation. Consistent with this notion, Gene
221 Ontology enrichment analysis for the *TNF*+ *GZMK*+ cluster produced top enriched terms including
222 "inflammatory response" (GO:0006954), "cellular response to cytokine stimulus" (GO:0071345), and "positive
223 regulation of chemokine (C-X-C motif) ligand 2 production" (GO:2000343) (Extended Data Fig. 5f).

224 To investigate the hypothesis that *TNF*+ *GZMK*+ CD8 T cells can instruct NF-κB inflammation in tumour
225 cells, we examined the correlation between frequencies of the *TNF*+ *GZMK*+ or *GZMB*+ Exhausted clusters in
226 each sample and the respective tumour cell-specific score of NF-κB activity based on an established gene set[53].
227 The change in the frequency of *TNF*+ *GZMK*+ cells before and after pembrolizumab therapy was positively
228 correlated with a change in NF-κB signaling score in tumour cells, whereas the analogous correlation was not
229 found for the *GZMB*+ Exhausted cluster (Fig. 5f,g). We then further hypothesized that a ratio of *TNF*+ *GZMK*+
230 cluster to the *GZMB*+ Exhausted cells would correlate with tumour NF-κB signaling. Analysis of on-treatment
231 samples identified two groups of patients whose log ratios were greater than 0 (higher *TNF*+ *GZMK*+ cluster,
232 group 2) or less than 0 (higher *GZMB*+ Exhausted cluster, group 1) (Fig. 5h). This ratio was positively correlated

233 with tumour NF-κB score, and tumour cells from samples in in group 2 had significantly higher tumour NF-κB
234 scores compared to those in group 1 (Fig. 5i). In summary, these results demonstrate that ICI treatment can induce
235 an expansion of a subset of inflammatory CD8 T cells characterized by *TNF* and *GZMK* expression that are
236 associated with increased tumour NF-κB signaling.
237
238 ICI treatment failure in patients with MSI-H cancers is associated with elevation of the neutrophil-to-lymphocyte
239 ratio in peripheral blood
240 Given the well-established limitations of standard single-cell RNA sequencing technologies to study
241 neutrophils[54], we sought to test our hypotheses regarding neutrophils using additional human datasets. Recently,
242 a multicellular and molecular inflammatory hub composed of NF-κB transcription factors, inflammatory tumour
243 cells, lymphocytes, neutrophils, and neutrophil-attracting chemokines has been described in human colorectal
244 cancer (COAD)[55]. We hypothesized that within a TME capable of upregulating such NF-κB-dependent,
245 neutrophil-recruiting inflammation, MSI-H status and the accompanying increased T cell infiltration[56,57] would
246 result in an increase in neutrophils in the TME. Inference of TME immune composition using CIBERTSORTx[58]
247 for analysis of the Cancer Genome Atlas (TCGA) RNA sequencing dataset for COAD patients, grouped by their
248 MSI status, showed an increase in neutrophils in a subset of MSI-H tumours compared to MSS tumours (Extended
249 Data Fig. 5f). We reasoned furthermore that, given the systemic mobilization of neutrophils during ICI resistance
250 in an antigen-rich tumour in mice (Fig. 3b), ICI resistance in patients with MSI-H cancers may be associated with
251 exacerbated systemic neutrophilia after treatment. We identified MSI-H cancers in our institutional next
252 generation sequencing database, and analyzed those who were started on ICI therapy but experienced treatment
253 failure. When compared to a 6-week period prior to initiation of ICIs, the peripheral blood neutrophil to
254 lymphocyte ratio (NLR) was increased after ICI treatment in the period preceding disease progression (Fig. 5i).
255 NLR has been associated with poor prognosis in various human cancer types, including but not exclusive to MSI-
256 H cancers[59,60]. Our findings provide additional evidence in support of the proposed ICI resistance mechanism in
257 tumours with T cell inflammation.
258

259

260 **Discussion**

261 In this study, we define a mechanism by which T cells instruct an NF-κB inflammation circuit involving
262 tumour cells and neutrophils, which exacerbates an immunosuppressive TME and results in resistance to ICI
263 therapy. NF-κB is a signaling pathway activated in many cell types in the TME and is known to both promote
264 and prevent tumour progression depending on context[11]. NF-κB signaling in cancer and myeloid immune cells,
265 however, predominantly result in pro-tumour inflammation during tumourigenesis and progression[61,62]. Notably,
266 inhibition of TNFα has recently been shown to improve ICI efficacy in mouse models, in addition to protecting
267 against autoimmune adverse effects[23,24]. A phase I clinical trial testing the strategy to combine TNFα blockade
268 and ICIs in cancer patients is underway[63]. However, TNFα can be produced by many cell types[50], and therefore
269 it has remained unclear to what extent T cells contribute to the effects of TNFα inhibition against cancer. Our
270 data show that T cell-derived TNFα can potentiate the production of NF-κB-regulated soluble factors that promote
271 adaptive resistance to therapy, and suggest that a subset of patients who may particularly benefit from ICIs and
272 TNFα blockade are those with T cell-inflamed tumours and baseline or ICI-induced NF-κB activity in tumour
273 and myeloid immune cells.

274 To our knowledge, we report for the first time an ICI resistance circuit requiring conventional CD4 T cells
275 and CD8 T cells activated by immunotherapy, which drive immunosuppressive inflammation in the TME. In
276 cancer immunity, various T cell subsets have been implicated in tumour development and progression, most
277 notably Tregs, which classically suppress effector T cell responses[64]. Th17 CD4 as well as γδ T cells can also
278 drive pro-tumour inflammation via IL-17 production[65,66], while CD8 T cells have been previously shown to
279 promote chemical carcinogenesis[67,68]. Interestingly, in the context of autoimmunity and immune-related adverse
280 events, effector memory CD4 T cells have been recently shown to instruct NF-κB inflammation in partnering
281 dendritic cells in a TNFR- and CD40-dependent manner[69,70]. We now show that ICI treatment can result in CD4
282 and CD8 T cell-driven immunosuppressive inflammation, which is dependent on IL-1R signaling and host-
283 derived TNFα. This T cell-dependent circuit has important therapeutic implications by informing novel strategies
284 that convert tumour-promoting T cell activity into anti-tumour immunity.

285 Our study also revises the current paradigm of ICI efficacy and offers a potential explanation for why
286 patients may experience poor responses to ICIs despite predicted or confirmed T cell infiltration. Importantly,
287 while demonstrated high T cell infiltration or proxy measures for T cell inflammation such as high tumour
288 mutational burden or MMRd/MSI-H status generally correlate with a relative improvement in ICI responses as
289 compared to non-T cell inflamed controls, it is notable that often, the majority of patients in the high T cell
290 inflammation group still do not respond to therapy[37,71,72]. Our findings now refine the current models of ICI
291 response to include the active role that tumour-infiltrating CD4 and CD8 T cells can play in shaping the TME,
292 including unexpectedly exacerbating an immunosuppressive tissue environment.

293 Analysis of human single cell RNA sequencing data from breast cancer patient samples collected before
294 and after anti-PD1 treatment with pembrolizumab confirmed that *TNF*-expressing CD8 T cell subsets increase
295 following ICI in humans. These cells were phenotypically similar to mouse CD8 T cells in the resistant AT3 MSI-
296 H tumours and distinct from *GZMB*-expressing exhausted effector cells, which expressed genes associated with
297 cytotoxicity. Expansion of *TNF*+ *GZMK*+ CD8 T cells was associated with increased NF-κB activity in tumour
298 cells, while *GZMB*+ exhausted effector T cells were not. These results suggest that *TNF*+ *GZMK*+ CD8 T cells
299 may contribute to increasing NF-κB-dependent tumour inflammation following ICI therapy in humans.
300 Furthermore, we found that neutrophils, which mobilize in response to NF-κB inflammatory
301 cytokines/chemokines from the TME in our mouse model of treatment resistance, are also elevated during ICI
302 resistance in colorectal MSI-H cancer patients. These data strongly support the mechanism of T cell-instructed
303 tumour-promoting inflammation we functionally define in mice.

304 In summary, our data elucidate a mechanism by which T cells can promote ICI resistance in a manner
305 dependent on the tumour context. These results are likely to inform new strategies for therapy selection and
306 immune monitoring as well as therapeutic strategies to convert inflammation-promoting T cell activity into
307 productive anti-tumour immunity.

308

309

310

311 **Methods**

312 Cell lines

313 Parental AT3 cells were gifted by Dr. Ross Levine (Memorial Sloan Kettering Cancer Center). B16F10
314 cells were gifted by Dr. Jeffrey Bluestone (University of California, San Francisco (UCSF)). 4T1 cells were gifted
315 by Dr. Mary Helen Barcellos-Hoff (UCSF). EO771 cells were gifted by Dr. Robin Anderson (Peter MacCallum
316 Cancer Centre). Moc1 cells were gifted by Dr. Patrick Ha (UCSF) and Dr. Ravindra Uppaluri (Dana Farber
317 Cancer Institute). AT3 and B16F10 parental and derivative cell lines were cultured in DMEM. 4T1 and EO771
318 parental and derivative cell lines were cultured in RPMI 1640. All media were supplemented with 10% fetal calf
319 serum, 10mM HEPES, and 100 U mL^{-1} penicillin and 100 μg mL^{-1} streptomycin. For generation of MSH2 knock
320 out cell lines, a combination of two targeting guide crRNAs (Dharmacon), or scrambled nontargeting control,
321 were mixed with tracrRNA and recombinant Cas9 protein (QB3 Macrolab) at 1:1:2:2 molar ratio and incubated
322 at 37°C to form the ribonucleoprotein complex. This was then mixed with 1ul of 100uM single-stranded
323 oligodeoxynucleotides (ssODN) enhancer, and 3 x 10^5 trypsinized cells in electroporation buffer and
324 electroporated using the Lonza 4D 96-well electroporation system. Nucleic acid sequences, electroporation buffer
325 type and electroporation code are found in Supplementary Table 1. After a 15 minute recovery in a 37°C CO2
326 incubator, cells were expanded in culture at subculture ratios of 1:10-1:15 every 48 hours. MSI-H cell lines used
327 have undergone 55-60 passages in total. Cell doubling times were quantified by culturing cells for 40-48 hours
328 and using the formula, doubling time = $\frac{duration\ x \log(2)}{\log(Final\ cell\ number) - \log(Seeding\ cell\ number)}$.

329

330 Animals and *in vivo* treatments

331 All mice were housed in an American Association for the Accreditation of Laboratory Animal Care-
332 accredited animal facility and maintained in specific pathogen-free conditions. Animal experiments were
333 approved by and conducted in accordance with Institutional Animal Care & Use Program protocol AN184195.
334 Female C57BL/6J and BALB/cJ mice between 8 and 12 weeks old were purchased from the Jackson Laboratory.
335 B16F10 (1 x 10^5 cells per 100 μL), AT3 (5 x 10^5 cells per 100 μL), EO771 (5 x 10^5 cells per 100 μL), 4T1 (5 x
336 10^5 cells per 100 μL), and Moc1 (3.5 x 10^6 cells per 100 μL) cells in serum-free DMEM were transplanted into

337 the right subcutaneous flank for B16F10 melanoma, and the left 4th mammary fat pad for breast cancer lines (AT3,
338 EO771, 4T1). Female B6.129S-*Tnf*^{tm1Gkl}/J mice (strain #005540; *Tnf*-KO in manuscript) between 7-8 weeks of
339 age were purchased from the Jackson Laboratory. Female B6.129X1(Cg)-*Csf3r*^{tm1Link}/J mice (strain #017838)
340 heterozygotes were purchased from the Jackson Laboratory and were used to breed *Csf3r* WT/WT and KO/KO
341 mice. TCR transgenic OT-I CD45.1 mice were bred at our facility. Animals were housed under standard specific
342 pathogen-free conditions with typical light/dark cycles and standard chow.

343 For all anti-PD-1 and anti-CTLA4 antibody treatments, 250 µg of anti-PD-1 clone RMP1-14 (Bio X Cell)
344 and 200 µg of anti-CTLA4 clone 9H10 (Bio X Cell) in 100 µL PBS were injected intraperitoneally at days 3, 6,
345 9 and 12 post tumour injection. For Moc1 tumour experiments, mice were treated with 250 µg of anti-PD-1
346 antibody every 3 days for 3 injections, upon tumours reaching 100 mm^3 in volume. For IL-1R inhibition, 200 µg
347 of antibody clone JAMA-147 (Bio X Cell) was injected intraperitoneally every 3 days starting at day 3 post
348 tumour injection. For Thy1 depletion, 200 µg of antibody clone M5/49.4.1 (Bio X Cell) was injected
349 intraperitoneally at days -2, 0, 7 and 14 relative to tumour injection. For anti-CD4 and anti-CD8 antibody
350 treatments, 400 µg of each antibody was injected intraperitoneally on days -1, 3, 7, 10, 13, and 16 post tumour
351 injection. For etanercept treatments, 400 mg of etanercept (Sigma-Aldrich) diluted in PBS was injected
352 intraperitoneally every 3 days starting on day of tumour injection.

353

354 <u>MSI PCR quantification</u>

355 Microsatellite instability in the mouse cell lines was quantified using a panel detecting four microsatellite
356 markers[36]. Genomic DNA from cell pellet was isolated using the GeneJET Genomic DNA Purification Kit
357 (Thermo Fisher Scientific) according to manufacturer protocol. 20 ng of genomic DNA was used as input for a
358 PCR reaction using Platinum Taq (Thermo Fisher Scientific) with 2mM MgCl2, 0.2 µM each primer, and 200
359 µM dNTP. The cycling profile included: 1 cycle at 94 °C for 4 minutes, 94 °C for 30 seconds, 56 °C for 45
360 seconds and 72 °C for 30 seconds for a total of 35 cycles, and a final extension at 72 °C for 6 minutes. Samples
361 were submitted for fragment analysis by Genewiz, and analyzed using PeakScanner 2 (Thermo Fisher Scientific).

362

363 Next generation sequencing and neoantigen priority score analysis

364 Whole exome and RNA sequencing was performed with flash frozen cell pellet submitted to MedGenome
365 (Foster City, CA). For whole exome sequencing, the library was prepared using the Agilent SureSelectXT Mouse
366 All Exon Kit, and sequenced on NovaSeq 6000 with paired-end 100 read length. Data was processed using Fastq
367 preprocessing using FastQC v0.11.8 and adapter trimming with fastq-mcf v1.05. 99.66% of the total reads aligned
368 to the reference genome. 87.77% of the aligned reads passed the alignment filter (mapping quality ≥ 29 and insert
369 size between 100-1000). Reads after duplicate removal, indel realignment and recalibration featured more than
370 98.49% coverage and 86.67-114.47X average depth. Somatic variant calling was performed using Strelka[73]
371 (v2.9.10). Default settings were used for variant calling. For realignment and base-recalibration, dbsnp150
372 variants were used. The identified somatic variants were further filtered and only passed and on-target variants
373 were considered for downstream analysis. Default parameters provided by Strelka were used to filter passed
374 somatic variants. The on-target variants were filtered based on the coordinates of the target regions provided by
375 the vendor. RNA sequencing was performed using two biological replicates per cell line using Illumina TruSeq
376 Stranded Total RNA library preparation, and sequenced using NovaSeq with target of 50 million total reads per
377 sample. 86.18-91.46% of total reads for each sample had Quality scores of > 30. Kallisto[74] (v0.46.1) was used to
378 quantify abundances of the transcripts in transcripts per million (TPM) with the strand specific read processing
379 argument '--rf-stranded'.

380 For neoantigen priority score analysis, the MuPeXI pipeline was used as described[38]. The somatic allele
381 frequency estimate was extracted from the strelka vcf records following the Strelka user guide and added to the
382 vcf files. The vcf files with allele frequency, the mean expression output files from Kallisto and the GRCm38
383 references were given as input to the MuPeXI pipeline (v1.2.0) with the species option set to mouse and the HLA
384 alleles set to 'H-2-Kb,H-2-Db'.

385

386 Mass cytometry antibodies

387 All mass cytometry antibodies and staining concentrations are listed in Supplementary Table 3. Primary
388 conjugates of mass cytometry antibodies were prepared using the Maxpar antibody conjugation kit (MCP9 for

389 Cadmium or X8 for non-Cadmium metals; Fluidigm) according to the manufacturer's recommended protocol.
390 After labeling, antibodies were diluted in HRP-Protector Peroxidase Stabilizer (Candor) for Cadmium conjugated
391 antibodies, and Candor PBS Antibody Stabilizer supplemented with 0.02% sodium azide for non-Cadmium
392 conjugated antibodies. Antibodies were stored at 4°C long term. Each antibody clone and lot was titrated to
393 optimal staining concentrations using primary mouse samples.
394
395 Cell preparation
396 Tissue preparations from tumour, tumour-draining lymph node, spleen and lymph node were performed
397 simultaneously. After euthanasia of mouse by CO2 inhalation, peripheral blood was collected via cardiac puncture
398 and transferred into heparin-coated vacuum tubes. Blood was diluted into ACK lysis buffer, incubated for 3
399 minutes on ice then quenched with 10 mL PBS with 5 mM ethylenediaminetetraacetic acid (EDTA) and 0.5%
400 bovine serum albumin (BSA) (PBS/EDTA/BSA). Spleens and tumour-draining inguinal lymph nodes were
401 homogenized with a syringe pusher over 70 µm filter with PBS/EDTA. Tumours were finely minced and digested
402 in RPMI-1640 with 4 mg ml^{-1} collagenase IV (Worthington) and 0.1 mg ml^{-1} DNaseI (Sigma) in a scintillation
403 vial with a micro stir bar for 30 minutes at 37 °C. After digestion, cells were filtered twice over 70 µm filters with
404 PBS/EDTA. All tissue samples were centrifuged at 500 *g* for 5 minutes at 4°C, resuspended in PBS/EDTA, and
405 mixed 1:1 with PBS/EDTA containing 100 mM cisplatin (Enzo Life Sciences) for 60 seconds before quenching
406 1:1 with PBS/EDTA/BSA. Cells were centrifuged again, resuspended in PBS/EDTA/BSA at a density between
407 1 x 10^6 and 1 x 10^7 cells per mL, fixed for 10 minutes at room temperature using 1.6% formaldehyde (final),
408 washed twice with PBS/EDTA/BSA and frozen in 100ul buffer at -80°C. All samples were processed on ice with
409 buffers at 4 °C.
410
411 Mass cytometry
412 2 x 10^6 cells from tumour and 1 x 10^6 cells from other organs from each animal were barcoded with distinct
413 combinations of stable Pd isotopes in 0.02% saponin in PBS as previously described[75]. Cells were washed twice
414 with cell-staining media (PBS with 0.5% BSA and 0.02% NaN_3) and combined into a single 15 mL conical tube.

415 For staining, cells were resuspended in cell-staining media, blocked with FcX (Biolegend) for 5 minutes at room
416 temperature, then incubated for 30 minutes at room temperature on a shaker, with surface marker antibody
417 cocktail in 1 mL total volume for tumour, and 500 µL volume for other organs. Cells were washed in cell-staining
418 media then permeabilized with methanol for 10 minutes at 4 °C, then washed again in cell-staining media. Cells
419 were then incubated with intracellular antibody cocktail in the same volume as surface markers for 30 minutes at
420 room temperature on a shaker. Cells were washed in cell-staining media then incubated with 1 mL PBS containing
421 1:5000 Iridium intercalator (Fluidigm) and 4% final formaldehyde. Cells were maintained in this final buffer for
422 2 days prior to sample acquisition on a CyTOF 2 mass cytometer (Fluidigm) using Maxpar Cell Acquisition
423 Solution. 1-5 x 10^5 cells were acquired per each sample. Data normalization was performed using EQ Four
424 Element Calibration Beads (Fluidigm) included during sample acquisition, using Normalizer v0.3 (Nolan lab).
425 Debarcoding was performed using Single Cell Debarcoder v0.2 (Nolan lab).
426
427 Mass cytometry data analysis
428 Immune cell subsets were manually gated using the strategy shown in Extended Data Fig. 6 (n=10 for
429 B16F10 conditions, n=5 for AT3 conditions). For CD8 T cell analysis, manually gated CD8 T cells were
430 subsampled to the analyzed dataset of 23120 cells. UMAP dimensionality reduction[39] was performed using all
431 available protein markers except Ki-67 and Ter119, using parameters of n_neighbors = 50, learning_rate = 0.5,
432 min_dist = 0.01, spread = 1. Phenograph[40] (v0.99.1) was used to compute cluster assignment, with k = 200.
433 Slingshot lineage inference[41] (v2.4.0) was performed using a matrix of UMAP1 and UMAP2 coordinates, with
434 starting cluster designated as cluster 9 (naïve CD8 T cells).
435 For pairwise correlation analysis involving neutrophil clusters, clusters were first identified using UMAP
436 and Phenograph using cells from each organ, with manual annotation of clusters representing neutrophils
437 (typically distinct group of cells in UMAP, CD11b+ Ly6G+). Cells from AT3 MSI-H or B16F10 MSI-H tumour
438 bearing animals were used for further analysis. For each sample, the cluster frequencies were calculated (percent
439 of total singlets for tumour, and percent of live CD45+ cells for other organs). Spearman pairwise correlation was
440 performed, and filtered for correlations involving neutrophils with $r > 0.7$ or < -0.7.

441

442 Cytokine quantification

443 For quantification of cytokines from tumour, minced tumour was lysed using RIPA buffer containing
444 protease inhibitor (Cell Biolabs) on ice for 10 minutes, followed by centrifugation at 14,000 rpm for 10 minutes
445 at 4 °C. Supernatant containing cell lysate was collected and normalized to the same A595 using the Bio-Rad
446 Protein Assay. Samples were frozen and stored at -80 °C until quantification. For quantification of cytokines from
447 plasma, freshly isolated peripheral blood was centrifuged for 10 minutes at 4 °C at 1000 *g*. 100 µL of supernatant
448 plasma was mixed 1:1 with 100 µL of PBS/EDTA, and frozen until quantification. For multiplex cytokine
449 quantification, lysates or plasma were submitted for mouse discovery assays available through Eve Technologies
450 (Calgary, AB). For G-CSF ELISA, tumour lysates were analyzed using the mouse G-CSF ELISA Kit (Abcam
451 ab197743) per manufacturer protocol.

452

453 Principal component analysis

454 Principal component analysis was performed using manually gated cell frequencies (percent of singlets in
455 tumour) or cytokine concentrations as input. Values were log adjusted then analyzed using the function PCA from
456 the R package FactoMineR[76] (v2.4)

457

458 Flow cytometry and cell sorting

459 All flow cytometry antibodies and concentrations used for analysis is found in Supplementary Table 4.
460 Tissue samples were initially processed as for CyTOF, and cells were stained for viability with Zombie-NIR stain
461 (Biolegend). Cell surface staining was performed in cell-staining media (PBS with 0.5% BSA and 0.02% NaN_3)
462 for 20 minutes at room temperature. For intracellular staining, cells were permeabilized and fixed using
463 eBioscience Foxp3/Transcription Factor Staining Buffer Set prior to staining in 1X permeabilization buffer.
464 Stained cells were analyzed with a CytoFLEX flow cytometer (Beckman Coulter) or an LSR II flow cytometer
465 (BD Biosciences). Stained live cells were sorted using FACSAria cell sorters (BD Biosciences) using a 100 µm

466 nozzle and event rate of 3000-4000 per second into collecting vessels kept at 4 °C until downstream use. Gating
467 strategies are found in Extended Data Fig. 7.
468
469 In vitro cellular assays
470 For tumour-T cell co-culture, CD8 T cells and tumour cells were sorted as above. Prior to plating, 96 well
471 flat bottom plate wells were coated with anti-CD3 antibody (clone 145-2C11, 10 μg/mL final in PBS) for 4-6
472 hours at 37°C and washed twice with PBS. For each cell population in the co-culture, 3.5 x 10^4 cells were plated
473 together with anti-CD28 antibody (clone 37.51, 3 μg/mL final) and any neutralizing antibodies in 200 μL final
474 volume of T cell media (RPMI 1640 with 10% FCS, 25mM HEPES, 2mM L-glutamine, 33μM 2-mercaptoethanol,
475 100 U mL^{-1} penicillin and 100 μg mL^{-1} streptomycin. After 24 hours of culture in a 37 °C incubator, the
476 supernatant was collected for G-CSF ELISA.
477 For OT-I T cell MDSC assay, neutrophils were sorted as above from AT3 MSI-H tumour, while OT-I
478 cells were harvested from spleen of OT-I CD45.1 mice by processing over a 70 μm filter. In 96 well U-bottom
479 plates, 1 x 10^5 OT-I splenocytes and 2.5 x 10^4 sorted neutrophils were combined with or without SIINFEKL
480 peptide at 0.4 ng/mL in 200 μL T cell media. Cells were incubated in a 37 °C CO2 incubator for 42 hours, then
481 BrdU was added to the wells at 10 μM final concentration for an additional 6 hours. Cells were collected and
482 stained with Zombie NIR, anti-TCRβ, anti-CD45.1, and anti-CD8a antibodies then anti-BrdU antibody as per
483 manufacturer protocol for the eBioscience BrdU Staining Kit for Flow Cytometry. Cells were analyzed using an
484 LSR II flow cytometer.
485 For assessment of G-CSF by ELISA following TNFα and/or IL-1α stimulation, 0.1 ng/ml of cytokine was
486 added to cell culture media 24 hours prior to collection of supernatant for analysis. For analysis of IκBα by flow
487 cytometry, TNFα and IL-1α (1 ng/ml) was added to culture media 20 minutes prior to cell harvest and processing
488 for staining and flow cytometry as above.
489
490 Quantitative reverse transcription PCR

491 Cells were sorted into 500 µL TRIzol reagent (Thermo Fisher Scientific). RNA was isolated using Direct-
492 zol 96 MagBead RNA kit (Zymo) per manufacturer protocol. cDNA was generated using Iscript Reverse
493 Transcription Supermix (Bio-Rad) per manufacturer protocol. Real-time PCR was performed using Taqman
494 primers for *Csf3* (Thermo Fisher Scientific Mm00438334_m1), *Cxcl1* (Mm04207460_m1), and *Gapdh*
495 (Mm99999915_g1) on a Bio-Rad C1000 Thermal Cycler. Delta delta Cq values were calculated against *Gapdh*
496 then against biological control.
497
498 Western blot
499 Protein lysates were generated using RIPA buffer containing protease inhibitor (Cell Biolabs) on ice for
500 10 minutes, followed by centrifugation at 14,000 rpm for 10 minutes at 4 °C. Supernatant containing cell lysate
501 was collected, and 20 µg of lysate was loaded onto NuPAGE 4-12% Bis-Tris protein gel (Thermo Fisher
502 Scientific). Gels were run in NuPAGE MOPS SDS running buffer, then transferred to a nitrocellulose blot in
503 NuPAGE Transfer Buffer. Blots were incubated with PBS-T (0.1% Tween 20) with 5% BSA, then incubated with
504 primary antibody against MSH2 (clone FE11, Thermo Fisher Scientific, 1:500 dilution) overnight at 4 °C. After
505 washing in PBST, HRP goat anti-mouse IgG secondary antibody was added in PBS-T and incubated for 1 hour.
506 Blot was developed using SuperSignal West Pico PLUS chemiluminescent substrate (Thermo Fisher Scientific)
507 and acquired using a Bio-Rad ChemiDoc system.
508
509 Human breast cancer single-cell RNAseq analysis
510 Data was obtained from https://lambrechtslab.sites.vib.be/en/single-cell and is deposited at the European
511 Genome-phenome Archive (EGA) under study no (EGAS00001004809) and under data accession
512 no. EGAD00001006608. Data was imported to Seurat (v. 4.1.0) as a Seurat Object. For quality control, the data
513 was previously filtered by excluding all cells expressing <200 or >6,000 genes, cells that contained <400 unique
514 molecular identifiers (UMIs), and cells with >15% mitochondrial counts. Raw counts were normalized using
515 sctransform (v. 0.3.3) and glmGamPoi (v. 1.2.0) with regression of cell cycle genes, percent mitochrondrial counts,
516 and number of UMIs (counts). Principal Component Analysis (PCA) was performed using variable genes. Cell

517 clusters were defined using Seurat's FindNeighbors (dim 1-20) and FindClusters (resolution 0.5) and were
518 visualized using Uniform Manifold Approximation and Projection (UMAP). Cluster annotations for major cell
519 types were provided in the metadata and aligned well with cluster assignment. The T cell cluster was fine
520 annotated into CD4, CD8, and Tregs based on expression of *CD4*, *CD8A*, *CD8B*, and *FOXP3*. The data was then
521 filtered to CD8 T cells only or tumour cells only.

522 CD8 T cells were reclustered using the above parameters. Clusters were defined using the FindAllMarkers
523 function in Seurat which identified differentially expressed genes (DEGs). Genes must be expressed in 25% of
524 cells. DEGs between specific clusters, found using FindMarkers, were plotted using EnhancedVolcano (v. 1.8.0).
525 For genes of interest, the density, or for two genes the joint density, was plotted in UMAP space using Nebulosa
526 (v. 1.0.2). DEenrichRPlot (Seurat and enrichR (v. 3.0)) was run to determine GO terms enriched in specific
527 clusters using the GO_Biological_Process_2021 list.

528 The proportion of cells in a given cluster from "Pre" or "On" treatment was calculated on a per patient
529 basis by normalizing for the number of CD8s per patient. The frequency of any cluster of CD8s compared "Pre"
530 vs "On" treatment was normalized to the number of cells in the entire tumour. Paired differences in cluster
531 frequency were tested using paired Wilcoxon.

532 Tumour cell scoring for NF-κB/TNFα signaling was performed using the gene set "HALLMARK_TNFA
533 SCORING_VIA_NFKB" obtained from Molecular Signatures Database or MSigDB and the AddModuleScore
534 function in Seurat. Differences in score were calculated "Pre" vs "On" treatment.

535 To determine the relationship between CD8 subsets and tumour NF-κB/TNFα signaling, the paired
536 difference in the frequency of each CD8 subset was calculated and correlated with the paired difference in tumour
537 NF-κB/TNFα signaling. Additionally, the log2 ratio of *TNF*+ *GZMK*+ CD8s to GZMB+ Exhausted CD8s on
538 treatment was calculated and correlated with on-treatment tumour NF-κB/TNFα signaling scores. Patients with
539 a log2 ratio < 0 were classified as Group 1 with more skew towards *GZMB*+ Exhausted CD8s. Patients with a
540 log2 ratio > 0 were classified as Group 2 with more skew towards *TNF*+ *GZMK*+ CD8s. The on-treatment tumour
541 NF-κB/TNFα signaling score for these binned patients were compared via Mann-Whitney non-parametric test.
542 Spearman correlation was used for all correlations due to lack of normality in the data (tested using Shapiro-Wilk).

543

544 CIBERSORTx analysis

545 COAD bulk RNA sequencing data from TCGA was analyzed using the CIBERTSORTx[58] platform
546 (cibersortx.stanford.edu). Proportion of neutrophils as percentage of immune cells in sample was deconvoluted
547 using the LM22 signature matrix and default parameters. MSIsensor[77] scores for each tumour sample was used
548 to stratify patients as MSS or MSI-H using a published dataset[10].

549

550 Human peripheral blood neutrophil to lymphocyte ratio analysis

551 Patients with MSI-H tumours from our institutional database of tumours submitted for next generation
552 sequencing were identified. Dataset was further filtered to non-central nervous system tumours and patients
553 receiving ICI therapy (included single or combinations of pembrolizumab, nivolumab, atezolizumab, or
554 ipilimumab) during their course of treatment. Among this group of patients, those who experienced radiologist-
555 confirmed imaging-based progression were identified, with the date of progression defined as the date of imaging.
556 6-week averaged values were derived from all available complete blood count with differential lab testing prior
557 to initiation of immunotherapy or prior to progression of disease. For each patient and timepoint, the absolute
558 neutrophil count was divided by the absolute lymphocyte count to derive the neutrophil to lymphocyte ratio (NLR).

559

560 Statistical analyses

561 Unless otherwise indicated, statistical testing was performed using GraphPad Prism (9.4.0). Prior to
562 significance testing for differences among groups, the normality of data distribution for each group being tested
563 was tested via Shapiro-Wilk test, where data with $p > 0.05$ were considered normally distributed. For normal
564 datasets, t test was performed, with Welch's correction if F test demonstrated unequal SD between groups. For
565 non-normal datasets, Mann-Whitney U test was used. Multiple testing correction was performed using Holm-
566 Sidak method to generate adjusted p values where indicated. All data points represent biological replicates.

567

568

Data availability

Data will be deposited into Mendeley Data and also available by request to the senior author without restrictions.

Code availability

R code for analyses performed within the manuscript will be made available upon request.

References

1. Sharma, P., Hu-Lieskovan, S., Wargo, J. A. & Ribas, A. Primary, Adaptive, and Acquired Resistance to Cancer Immunotherapy. *Cell* **168**, 707–723 (2017).
2. Zhang, L. *et al.* Intratumoral T Cells, Recurrence, and Survival in Epithelial Ovarian Cancer. *New England Journal of Medicine* **348**, 203–213 (2003).
3. Galon, J. *et al.* Type, density, and location of immune cells within human colorectal tumors predict clinical outcome. *Science (1979)* **313**, 1960–1964 (2006).
4. Tumeh, P. C. *et al.* PD-1 blockade induces responses by inhibiting adaptive immune resistance. *Nature* **515**, 568–571 (2014).
5. Waldman, A. D., Fritz, J. M. & Lenardo, M. J. A guide to cancer immunotherapy: from T cell basic science to clinical practice. *Nature Reviews Immunology 2020 20:11* **20**, 651–668 (2020).
6. Galon, J. & Bruni, D. Approaches to treat immune hot, altered and cold tumours with combination immunotherapies. *Nature Reviews Drug Discovery 2018 18:3* **18**, 197–218 (2019).
7. Le, D. T. *et al.* PD-1 Blockade in Tumors with Mismatch-Repair Deficiency. *New England Journal of Medicine* **372**, 2509–2520 (2015).
8. Le, D. T. *et al.* Mismatch repair deficiency predicts response of solid tumors to PD-1 blockade. *Science* **357**, 409–413 (2017).
9. Germano, G. *et al.* Inactivation of DNA repair triggers neoantigen generation and impairs tumour growth. *Nature* **552**, 1–5 (2017).
10. Mandal, R. *et al.* Genetic diversity of tumors with mismatch repair deficiency influences anti–PD-1 immunotherapy response. *Science (1979)* **364**, 485–491 (2019).
11. Shalapour, S. & Karin, M. Pas de Deux: Control of Anti-tumor Immunity by Cancer-Associated Inflammation. *Immunity* **51**, 15–26 (2019).
12. Giri, D. K. & Aggarwal, B. B. Constitutive Activation of NF-κB Causes Resistance to Apoptosis in Human Cutaneous T Cell Lymphoma HuT-78 Cells: AUTOCRINE ROLE OF TUMOR NECROSIS FACTOR AND REACTIVE OXYGEN INTERMEDIATES *. *Journal of Biological Chemistry* **273**, 14008–14014 (1998).
13. Wolf, J. S. *et al.* IL (interleukin)-1alpha promotes nuclear factor-kappaB and AP-1-induced IL-8 expression, cell survival, and proliferation in head and neck squamous cell carcinomas. *Clin Cancer Res* **7**, 1812–1820 (2001).
14. Karin, M. NF-κB as a Critical Link Between Inflammation and Cancer. *Cold Spring Harb Perspect Biol* **1**, a000141 (2009).
15. Xia, Y., Shen, S. & Verma, I. M. NF-κB, an Active Player in Human CancersNF-κB, an Active Player in Human Cancers. *Cancer Immunol Res* **2**, 823–830 (2014).

611 16. Wang, D. & Du Bois, R. N. Immunosuppression associated with chronic inflammation in the tumor
612 microenvironment. *Carcinogenesis* **36**, 1085–1093 (2015).
613 17. Greten, F. R. & Grivennikov, S. I. Inflammation and Cancer: Triggers, Mechanisms, and Consequences.
614 *Immunity* **51**, 27–41 (2019).
615 18. Taniguchi, K. & Karin, M. NF-κB, inflammation, immunity and cancer: coming of age. *Nature Reviews*
616 *Immunology 2018 18:5* **18**, 309–324 (2018).
617 19. Grinberg-Bleyer, Y. *et al.* NF-κB c-Rel Is Crucial for the Regulatory T Cell Immune Checkpoint in
618 Cancer. *Cell* **170**, 1096-1108.e13 (2017).
619 20. Li, T. *et al.* c-Rel is a myeloid checkpoint for cancer immunotherapy. *Nature Cancer 2020 1:5* **1**, 507–
620 517 (2020).
621 21. Lim, S. O. *et al.* Deubiquitination and Stabilization of PD-L1 by CSN5. *Cancer Cell* **30**, 925–939 (2016).
622 22. Lu, C. *et al.* p50 suppresses cytotoxic T lymphocyte effector function to regulate tumor immune escape
623 and response to immunotherapy. *J Immunother Cancer* **8**, e001365 (2020).
624 23. Perez-Ruiz, E. *et al.* Prophylactic TNF blockade uncouples efficacy and toxicity in dual CTLA-4 and
625 PD-1 immunotherapy. *Nature 2019 569:7756* **569**, 428–432 (2019).
626 24. Bertrand, F. *et al.* TNFα blockade overcomes resistance to anti-PD-1 in experimental melanoma. *Nature*
627 *Communications 2017 8:1* **8**, 1–13 (2017).
628 25. Blank, C. U. *et al.* Defining 'T cell exhaustion'. *Nature Reviews Immunology 2019 19:11* **19**, 665–674
629 (2019).
630 26. Tu, S. *et al.* Overexpression of Interleukin-1β Induces Gastric Inflammation and Cancer and Mobilizes
631 Myeloid-Derived Suppressor Cells in Mice. *Cancer Cell* **14**, 408–419 (2008).
632 27. Yu, J. *et al.* Noncanonical NF-κB Activation Mediates STAT3-Stimulated IDO Upregulation in Myeloid-
633 Derived Suppressor Cells in Breast Cancer. *The Journal of Immunology* **193**, 2574–2586 (2014).
634 28. Hu, X. *et al.* Transmembrane TNF-α Promotes Suppressive Activities of Myeloid-Derived Suppressor
635 Cells via TNFR2. *The Journal of Immunology* **192**, 1320–1331 (2014).
636 29. Achyut, B. R. *et al.* Canonical NFκB signaling in myeloid cells is required for the glioblastoma growth.
637 *Sci Rep* **7**, (2017).
638 30. Kim, T. M., Laird, P. W. & Park, P. J. The landscape of microsatellite instability in colorectal and
639 endometrial cancer genomes. *Cell* **155**, 858 (2013).
640 31. Le, D. T. *et al.* PD-1 Blockade in Tumors with Mismatch-Repair Deficiency. *New England Journal of*
641 *Medicine* **372**, 2509–2520 (2015).
642 32. Le, D. T. *et al.* Mismatch repair deficiency predicts response of solid tumors to PD-1 blockade. *Science*
643 *(1979)* **357**, 409–413 (2017).
644 33. Roudko, V. *et al.* Shared Immunogenic Poly-Epitope Frameshift Mutations in Microsatellite Unstable
645 Tumors. *Cell* **183**, 1634-1649.e17 (2020).
646 34. Westcott, P. M. K. *et al.* Mismatch repair deficiency is not sufficient to increase tumor immunogenicity.
647 *bioRxiv* 2021.08.24.457572 (2021) doi:10.1101/2021.08.24.457572.
648 35. Roth, T. L. *et al.* Reprogramming human T cell function and specificity with non-viral genome targeting.
649 *Nature* **13**, 27.
650 36. Woerner, S. M. *et al.* Detection of coding microsatellite frameshift mutations in DNA mismatch repair-
651 deficient mouse intestinal tumors. *Mol Carcinog* **54**, 1376–1386 (2015).
652 37. Petrelli, F., Ghidini, M., Ghidini, A. & Tomasello, G. Outcomes Following Immune Checkpoint Inhibitor
653 Treatment of Patients With Microsatellite Instability-High Cancers: A Systematic Review and Meta-
654 analysis. *JAMA Oncol* **6**, 1068–1071 (2020).
655 38. Bjerregaard, A. M., Nielsen, M., Hadrup, S. R., Szallasi, Z. & Eklund, A. C. MuPeXI: prediction of neo-
656 epitopes from tumor sequencing data. *Cancer Immunology, Immunotherapy* **66**, 1123–1130 (2017).
657 39. McInnes, L., Healy, J., Saul, N. & Großberger, L. UMAP: Uniform Manifold Approximation and
658 Projection. *J Open Source Softw* **3**, 861 (2018).
659 40. Levine, J. H. *et al.* Data-Driven Phenotypic Dissection of AML Reveals Progenitor-like Cells that
660 Correlate with Prognosis. *Cell* **162**, 184–197 (2015).
661 41. Street, K. *et al.* Slingshot: Cell lineage and pseudotime inference for single-cell transcriptomics. *BMC*
662 *Genomics* **19**, 1–16 (2018).

42. Cibrián, D. & Sánchez-Madrid, F. CD69: from activation marker to metabolic gatekeeper. *Eur J Immunol* **47**, 946–953 (2017).
43. Veglia, F., Sanseviero, E. & Gabrilovich, D. I. Myeloid-derived suppressor cells in the era of increasing myeloid cell diversity. *Nature Reviews Immunology* 1–14 Preprint at https://doi.org/10.1038/s41577-020-00490-y (2021).
44. Allen, B. M. *et al.* Systemic dysfunction and plasticity of the immune macroenvironment in cancer models. *Nat Med* **26**, 1125–1134 (2020).
45. Waight, J. D., Hu, Q., Miller, A., Liu, S. & Abrams, S. I. Tumor-Derived G-CSF Facilitates Neoplastic Growth through a Granulocytic Myeloid-Derived Suppressor Cell-Dependent Mechanism. *PLoS One* **6**, e27690 (2011).
46. Chakraborty, A. & Guha, S. Granulocyte Colony-Stimulating Factor/Granulocyte Colony-Stimulating Factor Receptor Biological Axis Promotes Survival and Growth of Bladder Cancer Cells. *Urology* **69**, 1210–1215 (2007).
47. Tsukuda, M. *et al.* A tumor cell line producing granulocyte colony-stimulating factor and an immune suppressive factor. *Biotherapy 1993 6:3* **6**, 217–223 (1993).
48. Yuan, M. *et al.* Tumor-derived CXCL1 promotes lung cancer growth via recruitment of tumor-associated Neutrophils. *J Immunol Res* **2016**, (2016).
49. Caldwell, J. & Emerson, S. G. IL-1α and TNFα act synergistically to stimulate production of myeloid colony-stimulating factors by cultured human bone marrow stromal cells and cloned stromal cell strains. *J Cell Physiol* **159**, 221–228 (1994).
50. Grivennikov, S. I. *et al.* Distinct and Nonredundant In Vivo Functions of TNF Produced by T Cells and Macrophages/Neutrophils: Protective and Deleterious Effects. *Immunity* **22**, 93–104 (2005).
51. Peppel, K., Crawford, D. & Beutler, B. A tumor necrosis factor (TNF) receptor-IgG heavy chain chimeric protein as a bivalent antagonist of TNF activity. *Journal of Experimental Medicine* **174**, 1483–1489 (1991).
52. Bassez, A. *et al.* A single-cell map of intratumoral changes during anti-PD1 treatment of patients with breast cancer. *Nat Med* **27**, 820–832 (2021).
53. Liberzon, A. *et al.* The Molecular Signatures Database Hallmark Gene Set Collection. *Cell Syst* **1**, 417–425 (2015).
54. Grieshaber-Bouyer, R. *et al.* The neutrotime transcriptional signature defines a single continuum of neutrophils across biological compartments. *Nat Commun* **12**, 2856 (2021).
55. Pelka, K. *et al.* Multicellular immune hubs and their organization in MMRd and MMRp colorectal cancer. *bioRxiv* 2021.01.30.426796 (2021) doi:10.1101/2021.01.30.426796.
56. Dolcetti, R. *et al.* High Prevalence of Activated Intraepithelial Cytotoxic T Lymphocytes and Increased Neoplastic Cell Apoptosis in Colorectal Carcinomas with Microsatellite Instability. *Am J Pathol* **154**, 1805–1813 (1999).
57. Phillips, S. M. *et al.* Tumour-infiltrating lymphocytes in colorectal cancer with microsatellite instability are activated and cytotoxic. *British Journal of Surgery* **91**, 469–475 (2004).
58. Newman, A. M. *et al.* Determining cell type abundance and expression from bulk tissues with digital cytometry. *Nat Biotechnol* **37**, 773–782 (2019).
59. Howard, R., Kanetsky, P. A. & Egan, K. M. Exploring the prognostic value of the neutrophil-to-lymphocyte ratio in cancer. *Sci Rep* **9**, 19673 (2019).
60. Nebot-Bral, L. *et al.* Overcoming resistance to αPD-1 of MMR-deficient tumors with high tumor-induced neutrophils levels by combination of αCTLA-4 and αPD-1 blockers. *J Immunother Cancer* **10**, e005059 (2022).
61. Betzler, A. C. *et al.* NF-κB and Its Role in Checkpoint Control. *International Journal of Molecular Sciences 2020, Vol. 21, Page 3949* **21**, 3949 (2020).
62. Lalle, G., Twardowski, J. & Grinberg-bleyer, Y. NF-κB in Cancer Immunity: Friend or Foe? *Cells 2021, Vol. 10, Page 355* **10**, 355 (2021).
63. Montfort, A. *et al.* Combining Nivolumab and Ipilimumab with Infliximab or Certolizumab in Patients with Advanced Melanoma: First Results of a Phase Ib Clinical Trial. *Clinical Cancer Research* **27**, 1037–1047 (2021).

715 64. Vignali, D. A. A., Collison, L. W. & Workman, C. J. How regulatory T cells work. *Nature Reviews*
716 *Immunology 2008 8:7* **8**, 523–532 (2008).
717 65. Dmitrieva-Posocco, O. *et al.* Cell-Type-Specific Responses to Interleukin-1 Control Microbial Invasion
718 and Tumor-Elicited Inflammation in Colorectal Cancer. *Immunity* **50**, 166-180.e7 (2019).
719 66. Coffelt, S. B. *et al.* IL-17-producing γδ T cells and neutrophils conspire to promote breast cancer
720 metastasis. *Nature 2015 522:7556* **522**, 345–348 (2015).
721 67. Roberts, S. J. *et al.* Characterizing tumor-promoting T cells in chemically induced cutaneous
722 carcinogenesis. *Proceedings of the National Academy of Sciences* **104**, 6770–6775 (2007).
723 68. Kwong, B. Y. *et al.* Molecular Analysis of Tumor-Promoting CD8+ T Cells in Two-Stage Cutaneous
724 Chemical Carcinogenesis. *Journal of Investigative Dermatology* **130**, 1726–1736 (2010).
725 69. Jain, A. *et al.* T cells instruct myeloid cells to produce inflammasome-independent IL-1β and cause
726 autoimmunity. *Nature Immunology 2019 21:1* **21**, 65–74 (2019).
727 70. Yogev, N. *et al.* CD4+ T-cell-derived IL-10 promotes CNS inflammation in mice by sustaining effector
728 T cell survival. *Cell Rep* **38**, 110565 (2022).
729 71. McGrail, D. J. *et al.* High tumor mutation burden fails to predict immune checkpoint blockade response
730 across all cancer types. *Annals of Oncology* **32**, 661–672 (2021).
731 72. Li, F. *et al.* The association between CD8+ tumor-infiltrating lymphocytes and the clinical outcome of
732 cancer immunotherapy: A systematic review and meta-analysis. *EClinicalMedicine* **41**, 101134 (2021).
733 73. Kim, S. *et al.* Strelka2: fast and accurate calling of germline and somatic variants. *Nat Methods* **15**, 591–
734 594 (2018).
735 74. Bray, N. L., Pimentel, H., Melsted, P. & Pachter, L. Near-optimal probabilistic RNA-seq quantification.
736 *Nat Biotechnol* **34**, 525–527 (2016).
737 75. Zunder, E. R. *et al.* Palladium-based mass tag cell barcoding with a doublet-filtering scheme and single-
738 cell deconvolution algorithm. *Nature Protocols 2014 10:2* **10**, 316–333 (2015).
739 76. Lê, S., Josse, J. & Husson, F. FactoMineR: An R Package for Multivariate Analysis. *J Stat Softw* **25**, 1–
740 18 (2008).
741 77. Niu, B. *et al.* MSIsensor: microsatellite instability detection using paired tumor-normal sequence data.
742 *Bioinformatics* **30**, 1015–1016 (2014).
743
744

745 **Acknowledgements**

746 We thank the UCSF Flow Cytometry Core and S. Tamaki for CyTOF maintenance. We thank E. Engleman and
747 J. Bluestone for cell lines. We thank A. Marson and T. Roth for CRISPR-Cas9 reagents, protocols and equipment.
748 We thank the UCSF Clinical Cancer Genomics Laboratory, Molecular Oncology Initiative, and D. Raleigh for
749 access to the UCSF cBioPortal dataset. This study makes use of publicly available data generated by the
750 Lambrechts group in the BioKey study. A full list of investigators who contributed to the generation of the data,
751 and the funding source is available at doi: 10.1038/s41591-021-01323-8/. The Lambrechts group is not
752 responsible for the analysis or interpretation of the data presented. This study was supported by NIH grants DP5
753 OD023056 and R01 DE032033 to M.H.S., the UCSF Prostate Cancer Program Pilot Award to N.W.C., and NIH
754 S10 OD018040 to procure the CyTOF mass cytometer. N.W.C. is supported by NIH grant T32 5T32AI007334-
755 33. K.J.H-G is supported by the Stanford Propel Postdoctoral Scholarship. R.D. is supported by NIH grant F31

CA265128. J.L.Y. is supported by an NSF GRFP fellowship. M.H.S. is an Investigator of the Parker Institute for Cancer Immunotherapy and of the Chan Zuckerberg Biohub.

Contributions

Conceptualization: N.W.C., S.M.G., and M.H.S.; experimental methodology: N.W.C., K.J.H-G., K.W., L.S.L., R.D., J.L.Y., N.A.A., I.T.; computational methodology: N.W.C., S.M.G., E.J.K., K.J.H-G., B.Y.N., M.H.S., investigation: all authors; writing, original draft: N.W.C., S.M.G.; writing, review and editing: all authors; funding acquisition: M.H.S. and N.W.C.; supervision: M.H.S.

Corresponding author

Correspondence to Matthew H. Spitzer.

Fig. 1: Mouse syngeneic MSI-H tumors demonstrate variable response to ICIs.

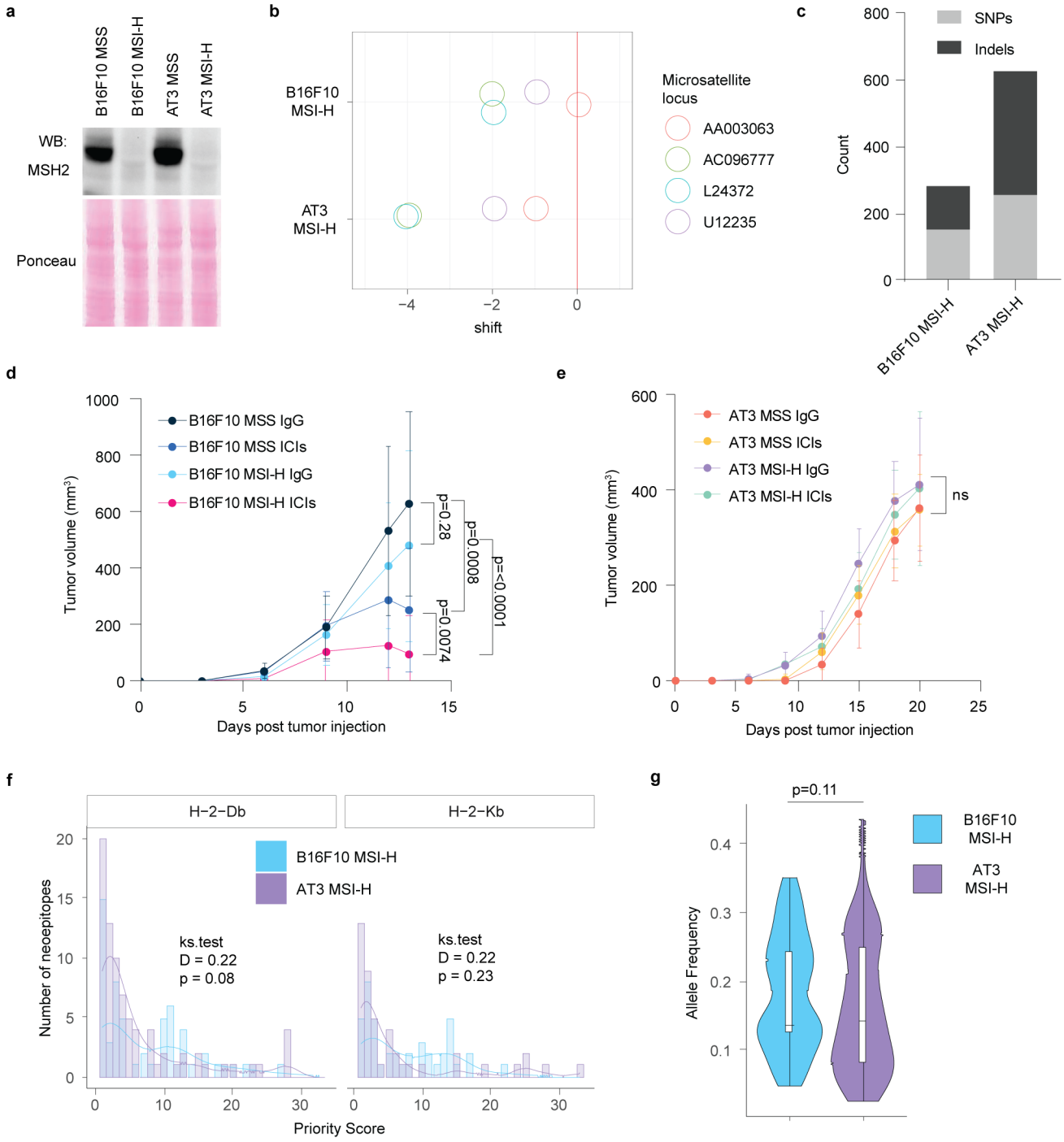

767

768 **Fig. 1: Mouse syngeneic MSI-H tumours demonstrate variable response to ICIs.**

769 **a,** Western blot of whole cell lysates of indicated cell lines. **b,** Targeted microsatellite PCR assay comparing
770 amplicon size at indicated loci for MSI-H vs. MSS cell line. **c,** Whole exome sequencing quantification of single
771 nucleotide polymorphisms (SNPs) and insertion-deletion mutations (indels) for indicated MSI-H cell lines
772 compared to the MSS lines. **d,** Quantification of mean volumes for B16F10 tumours treated with or without anti-
773 PD-1 and anti-CTLA4 antibodies (ICIs) at the indicated timepoints (arrowhead). n=15-18 mice per condition. **e,**
774 Same as in **(d)** but with AT3 cell lines. n=10-11 mice per condition. For **(d)** and **(e)**, Two-tailed p values are
775 calculated for day 20 tumour volumes using Mann-Whitney tests adjusted using Holm-Sidak. ns=not significant,
776 $p>0.05$. Bars represent SD. **f,** MuPeXI neoepitope affinity scores for indicated cell lines and HLA class. D statistic
777 and p values are calculated using a two-sided Kolmogorov-Smirnov test. **g,** Box and violin plots of neoepitope
778 allele frequencies in indicated cell lines. Two-tailed p value by Mann-Whitney test. Box plot: center line, median;
779 box limits, upper and lower quartiles; whiskers, 1.5x interquartile range.

Fig. 2: CD8 T cells increase in both ICI responsive and resistant tumors, but assume distinct phenotypic states

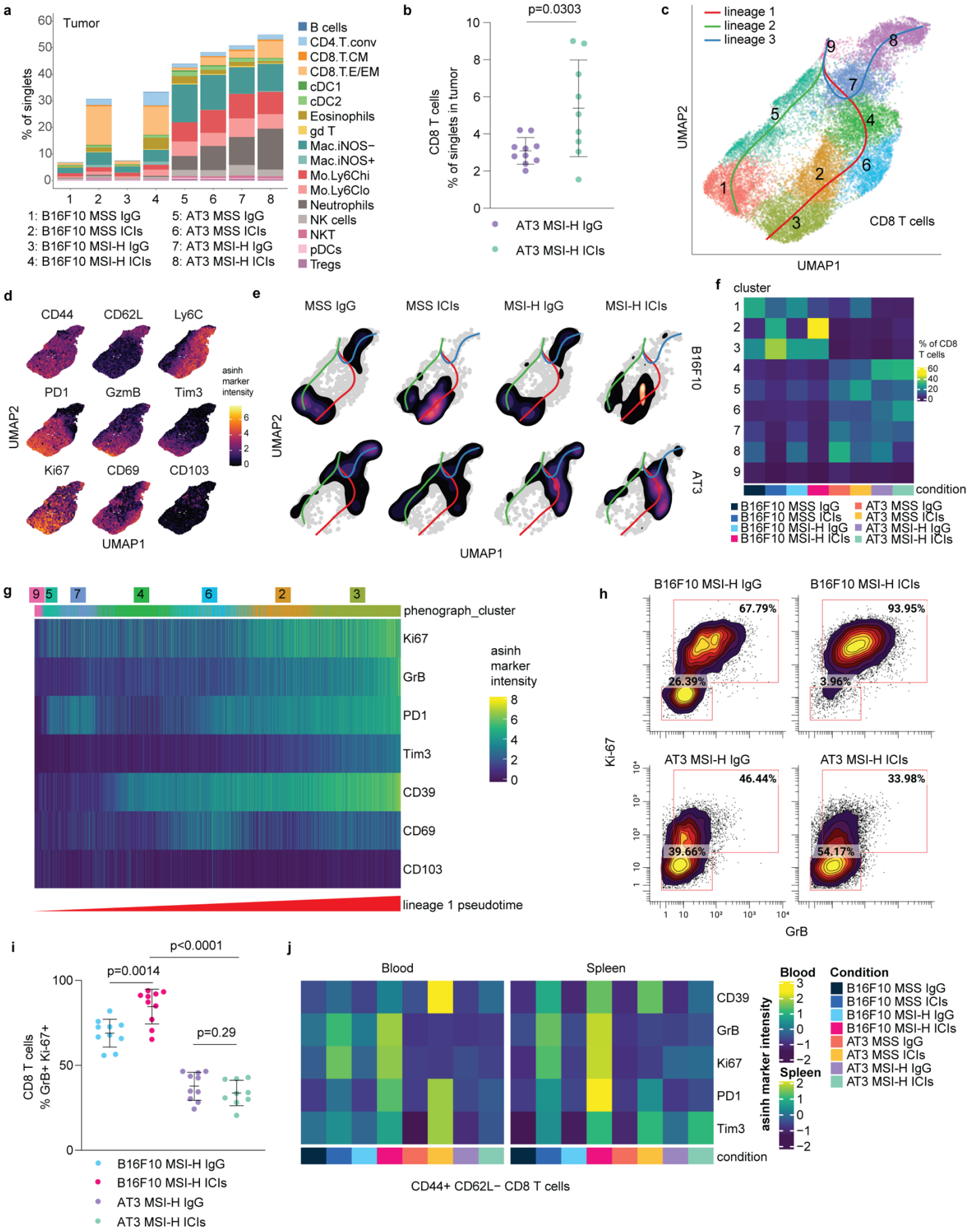

781 **Fig. 2: CD8 T cells increase in both ICI responsive and resistant tumours, but assume distinct phenotypic**
782 **states.**

783 **a,** Major immune cell populations in tumour were defined by manual gating of CyTOF data from indicated
784 tumours and treatment conditions. Conv=conventional; CM=central memory; E/EM=effector/effector memory;
785 Mac=macrophages; Mo=monocytes. Bar height for each population represents the mean of biological replicates
786 (n=10 for B16F10, n=5 for AT3 conditions) **b,** Quantification of CD8 T cell infiltration. Two-tailed p value by
787 Welch's t test. **c,** CD8 T cells from **(a)** analyzed by UMAP, Phenograph and Slingshot. Numbers represent
788 Phenograph clusters. Coloured lines represent Slingshot pseudotime lineages. **d,** Expression of selected markers
789 for cells in **(c)**. **e,** Cell density plots for cells in indicated conditions, with lineages denoted as in **(c)**. **f,** Heatmap
790 displaying mean % of CD8 T cells for each cluster and condition. **g,** Cells in lineage 1 are ordered by increasing
791 pseudotime, coloured by marker intensity. **h,** Representative biaxial plots of Granzyme B (GrB) and Ki-67+ CD8
792 T cells. **i,** Quantification of cells as analyzed in **(h)**. Center bar, mean. Upper and lower bars, SD. p values by two-
793 tailed t tests with Holm-Sidak multiple testing correction. **j,** Heatmap displaying mean of the median marker
794 intensities of cells in each mouse condition (n=10 for B16F10, n=5 for AT3 conditions) and organ.

Fig. 3: An NF-κB inflammatory program drives immunosuppresion in the ICI resistant TME

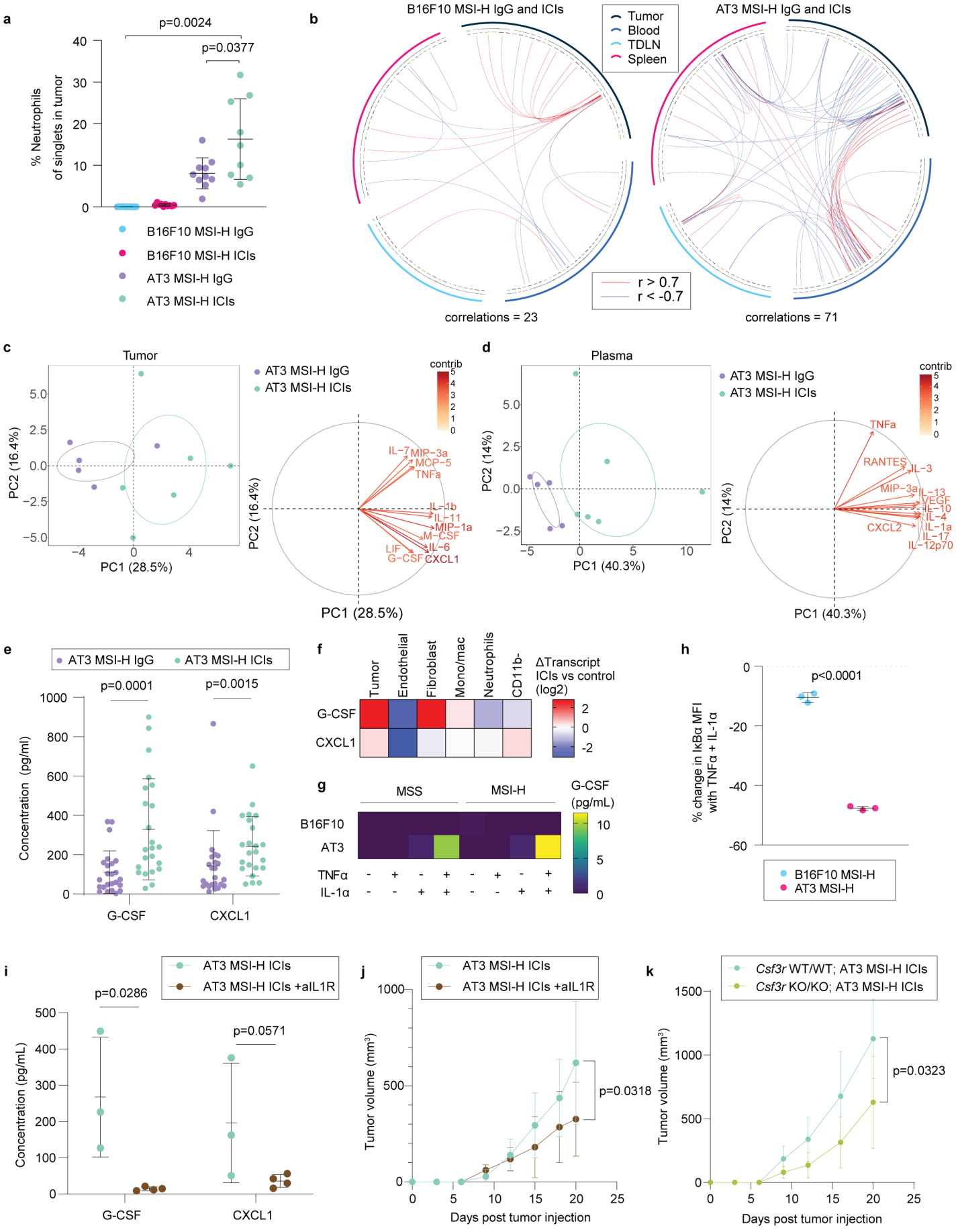

795

796 **Fig. 3: An NF-κB inflammatory program drives immunosuppression in the ICI resistant TME.**

797 **a,** Quantification of neutrophils in indicated tumour and treatment conditions. p values by two-tailed Welch t test
798 with Holm-Sidak multiple testing correction. **b,** Pairwise correlation of Phenograph clusters across organs, filtered
799 by those involving clusters identified as neutrophils and $r > 0.7$ or $r < -0.7$. **c,** Principal component analysis of
800 cytokines in tumour lysates detected by multiplexed bead assay. Ellipse, 95% confidence ellipse. Right, loadings
801 plot of contribution by the top 12 variables. **d,** Analysis as in **(c)** for cytokines in plasma. **e,** Quantification of
802 indicated cytokines in tumour lysates by multiplexed bead assay. Two-tailed p values by Mann-Whitney test. **f,**
803 qPCR of cytokine transcripts from sorted cells from AT3 MSI-H ICI treated tumours, with expression normalized
804 to control treated tumours. Values represent mean of 3-6 biological replicates. **g,** ELISA quantification of G-CSF
805 concentration in cell culture supernatant of indicated cell lines treated with or without indicated cytokines for 24h.
806 Data represent mean of 3 biological replicates. **h,** Quantification of IκBα median fluorescence intensity with or
807 without addition TNFa and IL-1α **i,** Quantification of cytokine concentrations in tumour lysates from indicated
808 conditions by multiplexed bead assay. p values by one-tailed Mann Whitney tests. **j,** Mean tumour volumes for
809 AT3 MSI-H tumours treated with indicated antibodies. p value by two-tailed t test of day 20 tumour volumes. **k,**
810 AT3 MSI-H mean tumour volumes when injected into mice with indicated genotypes and treated with ICIs. p
811 value of day 20 tumour volumes by two-tailed t test. n=5-7 mice. For all scatter plots, center bar, mean. Upper
812 and lower bars, SD.

Fig. 4: T cells drive activation of the inflammatory ICI resistance circuit

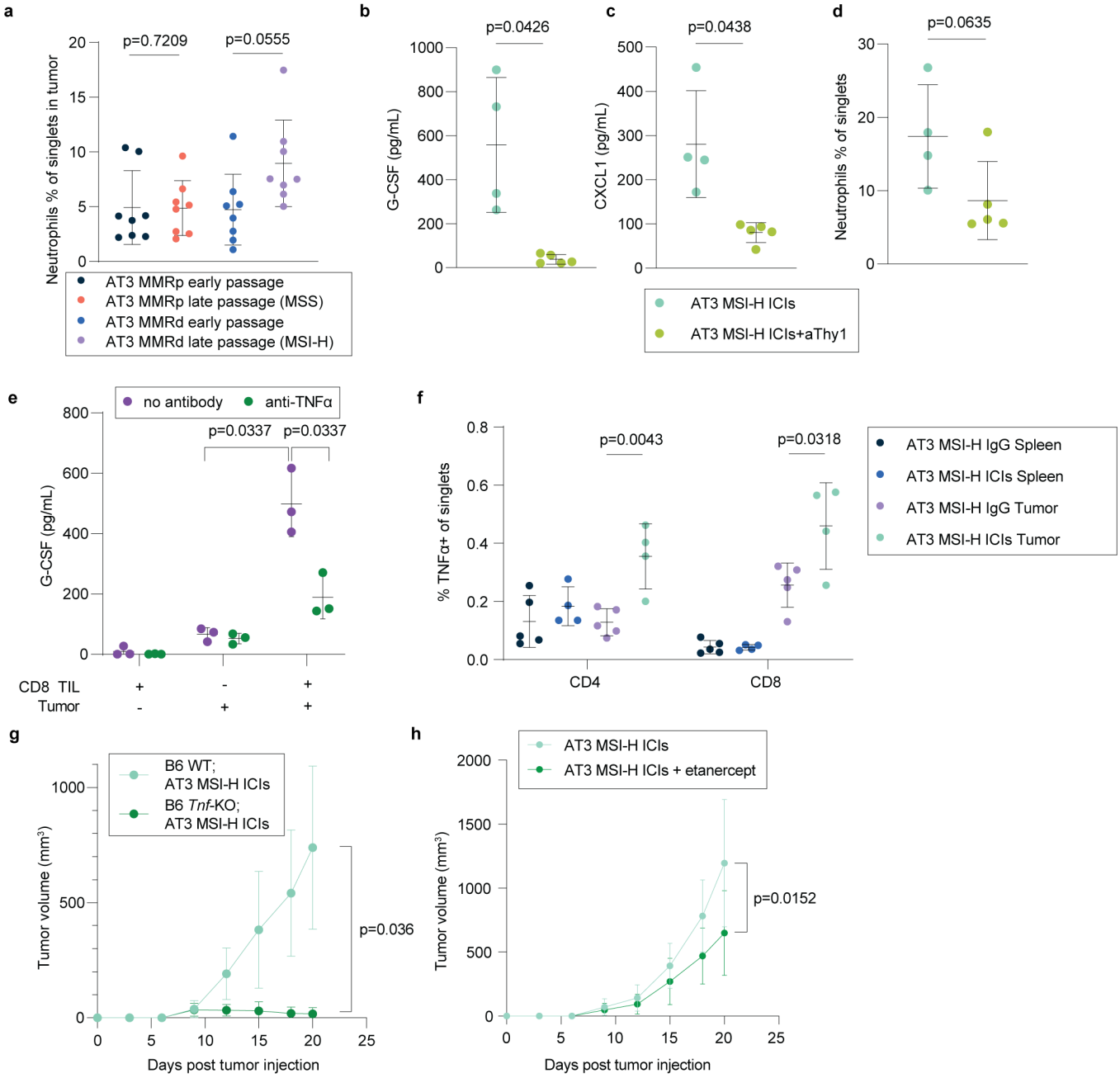

813

814 **Fig 4: T cells drive activation of the inflammatory ICI resistance circuit.**

815 **a,** Quantification of neutrophils in indicated AT3 mismatch repair-proficient (MMRp) or -deficient (MMRd)
816 tumours. Two-sided p values by Mann-Whitney test with Holm-Sidak multiple testing correction. **b,**
817 Quantification of G-CSF concentration in tumour lysates for indicated treatment conditions. p value by two-sided
818 Welch's t test. **c,** Quantification as in **(b)** for CXCL1. **d,** Quantification of neutrophils in tumour for indicated
819 treatment conditions. p value by two-sided Mann-Whitney test. **e,** Quantification of G-CSF concentration in
820 supernatant of 24h culture containing indicated sorted cell types from AT3 MSI-H tumours treated with ICIs,
821 with or without TNFα neutralizing antibody. p values by two-tailed Welch's t test and Holm-Sidak multiple
822 testing correction. **f,** Quantification of TNFα+ CD4 or CD8 T cells in tumour or spleen of AT3 MSI-H tumours
823 treated with indicated antibodies. p value by two-tailed t test. **g,** AT3 MSI-H tumour volumes when injected into
824 mice with indicated genotypes, with ICI treatment. p value of day 20 tumour volumes by two-tailed Mann-
825 Whitney test. **h,** ICI-treated AT3 MSI-H tumour volumes with or without etanercept treatment. p value of day 20
826 tumour volumes by two-tailed Mann-Whitney test. For all scatter plots, center bar, mean. Upper and lower bars,
827 SD.

Fig. 5: ICI-induced CD8 T cell, tumor, and neutrophil inflammation in human cancer.

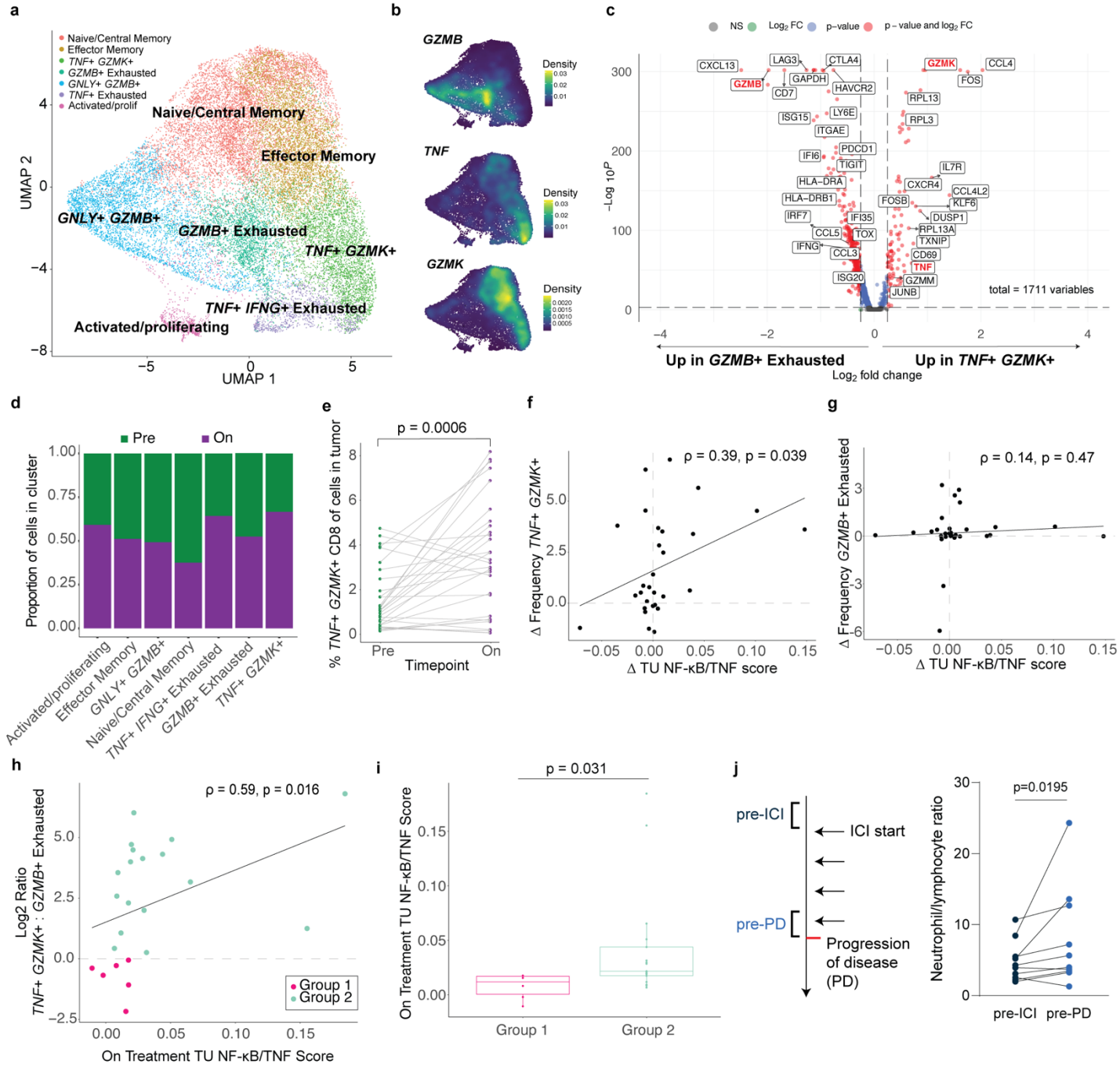

828

829 **Fig 5. ICI-induced CD8 T cell, tumour, and neutrophil inflammation in human cancer. a,** UMAP of 24,349
830 CD8 T cells colour coded by CD8 T cell phenotype (EGAS00001004809). **b,** UMAP cell density plots of *GZMB*,
831 *TNF*, and *GZMK* expression. **c,** Volcano plot of differential gene expression between *TNF*+*GZMK*+ CD8 and
832 *GZMB*+ Exhausted CD8 T cells. Genes of interest are highlighted in red. **d,** Stacked bar plot of proportion of cells
833 in each cluster originating from pre-treatment samples (Pre) vs. on-treatment (On). Proportions are normalized
834 for number of CD8 T cells per patient. **e,** Percent of cells in the *TNF*+*GZMK*+ cluster out of all cells in the tumour
835 for Pre vs On samples. Exact p value by two-tailed Wilcoxon matched-pairs signed rank test for paired samples
836 are shown. **f-g,** Spearman correlation analyses between the change in tumour NF-κB/TNFα signaling score and
837 change in frequency of *TNF*+ *GZMK*+ CD8 T cells **(f)** or *GZMB*+ Exhausted CD8 T cells **(g)** in each patient. **h,**
838 Spearman correlation analysis between the log2 ratio of the frequency of *TNF*+*GZMK*+ CD8 T cells to *GZMB*+
839 Exhausted CD8 T cells on treatment and the tumour NF-κB/TNFα signaling score on treatment. **i,** Boxplots
840 showing tumour NF-κB/TNFα signaling score on treatment for Group 1 (n=6) vs Group 2 (n=17). Exact p value
841 by two-tailed Mann-Whitney test is shown. Box plot: center line, median; box limits, upper and lower quartiles;
842 whiskers, 1.5x interquartile range. **j,** Definitional schema and paired plot of neutrophil/lymphocyte ratios in
843 peripheral blood of patients with MSI-H tumours treated with ICI therapy. Exact p value by two-tailed Wilcoxon
844 matched-pairs signed rank test.

Extended Data Fig. 1

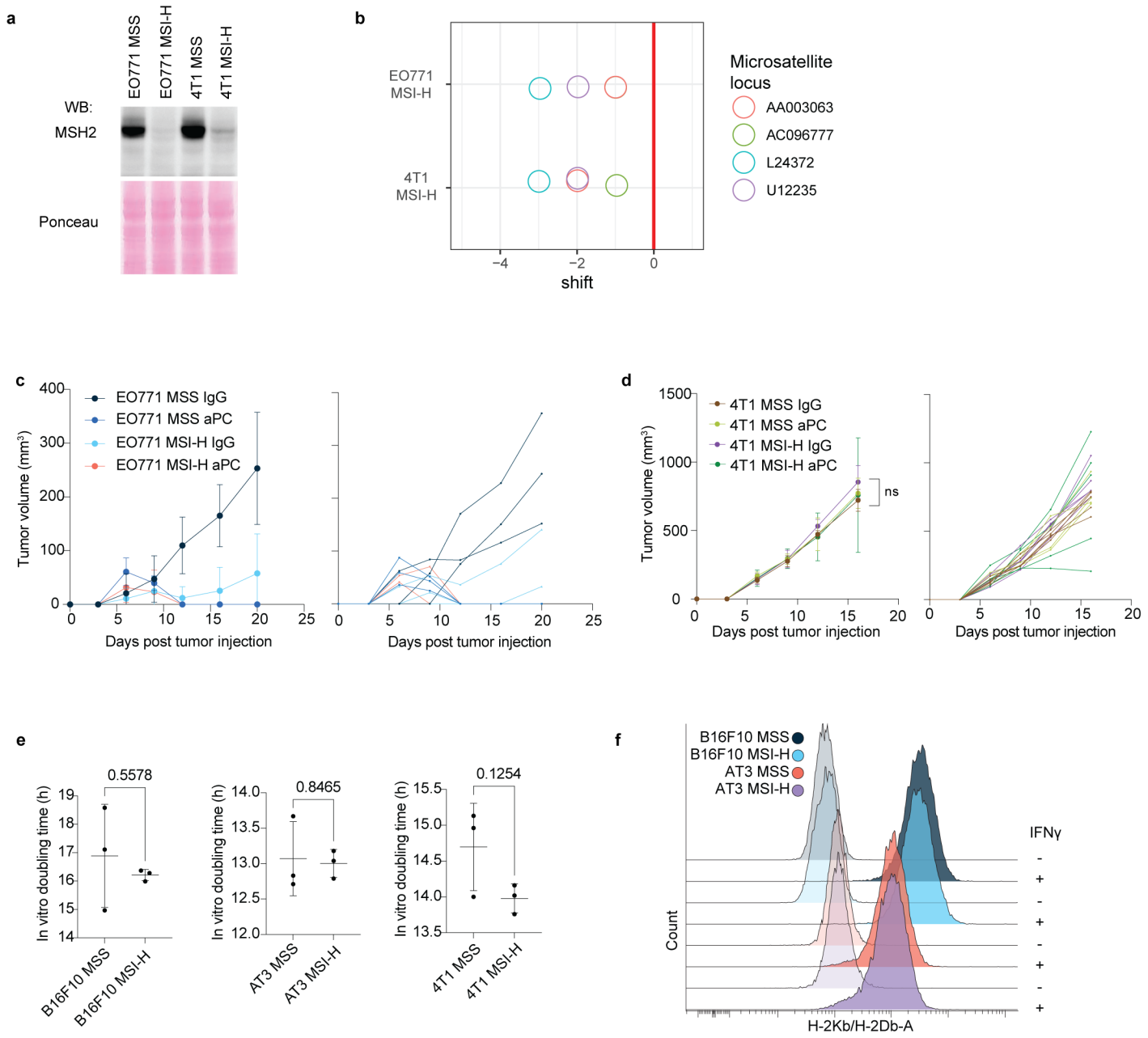

846 **Extended Data Fig. 1 Characteristics of mouse syngeneic tumours that demonstrate variable response to**
847 **ICIs.**

848 **a,** Western blot of whole cell lysates of indicated cell lines. **b,** Targeted microsatellite PCR assay comparing
849 amplicon size at indicated loci for MSI-H vs. MSS cell line**. c,** Left, quantification of mean volumes for EO771
850 tumours treated with or without anti-PD-1 and anti-CTLA4 antibodies (ICIs) at the indicated timepoints
851 (arrowhead). n=3 mice per condition. center point, mean; upper and lower bars, SD. Right, data for each mouse
852 **d,** analysis as in **(c)** with 4T1 tumours. ns, p>0.05 by two-tailed Mann-Whitney tests with Holm-Sidak multiple
853 testing correction. **e,** *In vitro* cell doubling times quantified for indicated cell lines. p values by two-tailed Mann-
854 Whitney test. Center line, mean; upper and lower bars, SD. **f,** Quantification of H-2Kb or H-2Db expression by
855 flow cytometry of indicated cell lines *in vitro* and treated with or without IFNγ (62.5 ng/mL for 48 hours).

Extended Data Fig. 2

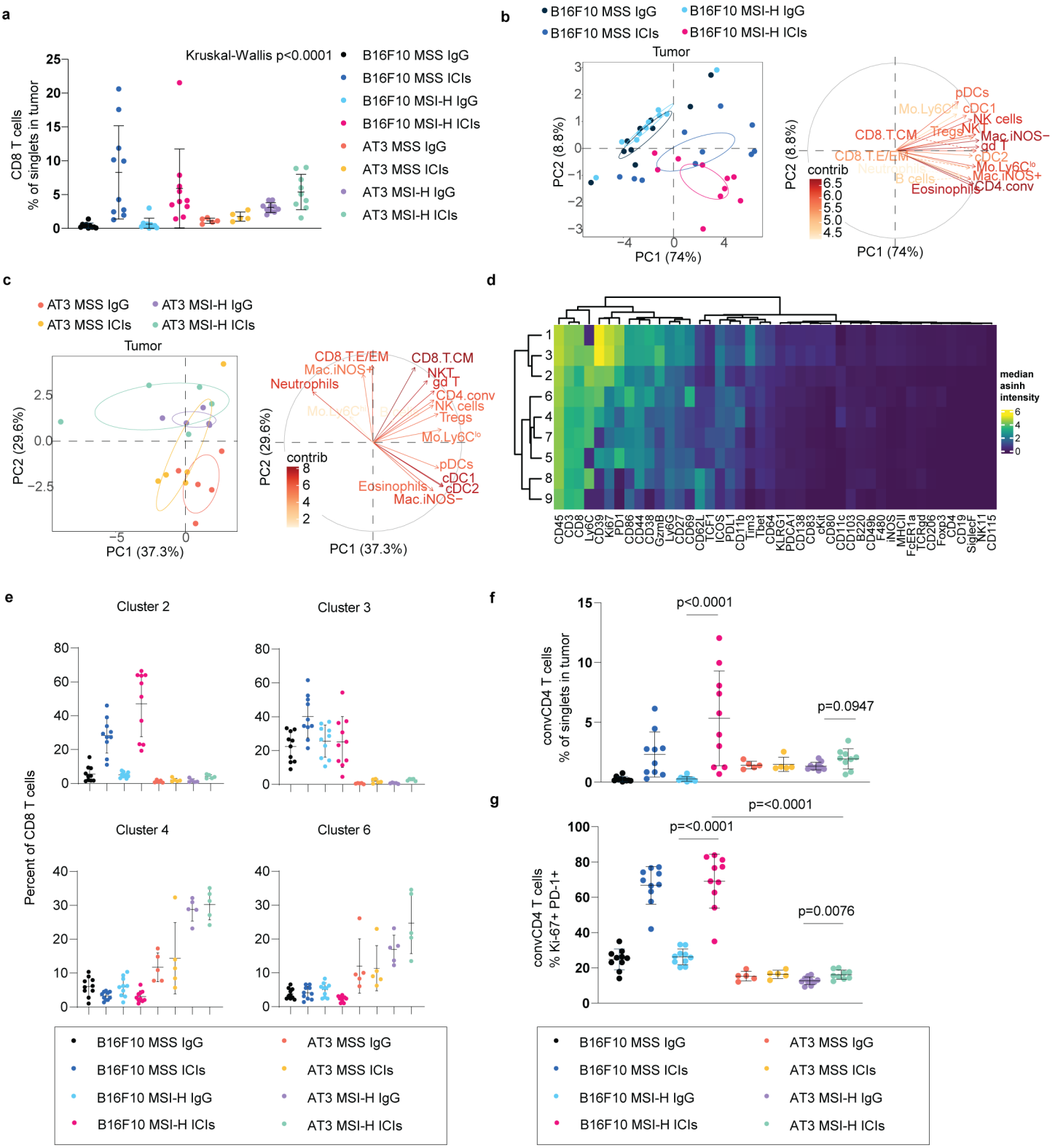

856

857 **Extended Data Fig. 2 T cells assume divergent phenotypes in mouse models of ICI resistance and response.**
858 **a,** Quantification of CD8 T cells in indicated tumour type and treatment condition. **b,** Principal component
859 analysis of manually gated cell type frequencies for indicated tumours and treatment conditions. Ellipse, 95%
860 confidence ellipse. Right, loadings plot of contribution by top 20 variables. **c,** Principal component analysis as in
861 **(b)** for AT3 tumours. **d,** Heatmap of median marker intensities for CD8 T cell clusters in Fig. 2c. Hierarchical
862 clustering is performed for both markers and clusters. **e,** Sample level quantification of cluster proportions by
863 condition for indicated CD8 T cell clusters. **f,** Quantification of conventional CD4 T cells in indicated tumour
864 types and treatment conditions. p values by two-tailed Mann-Whitney tests with Holm-Sidak multiple testing
865 correction. **g,** Analysis as in **(f)** for Ki-67 and PD-1 double-positive conventional CD4 T cells. For all scatter plots,
866 center bar, mean. Upper and lower bars, SD.

Extended Data Fig. 3

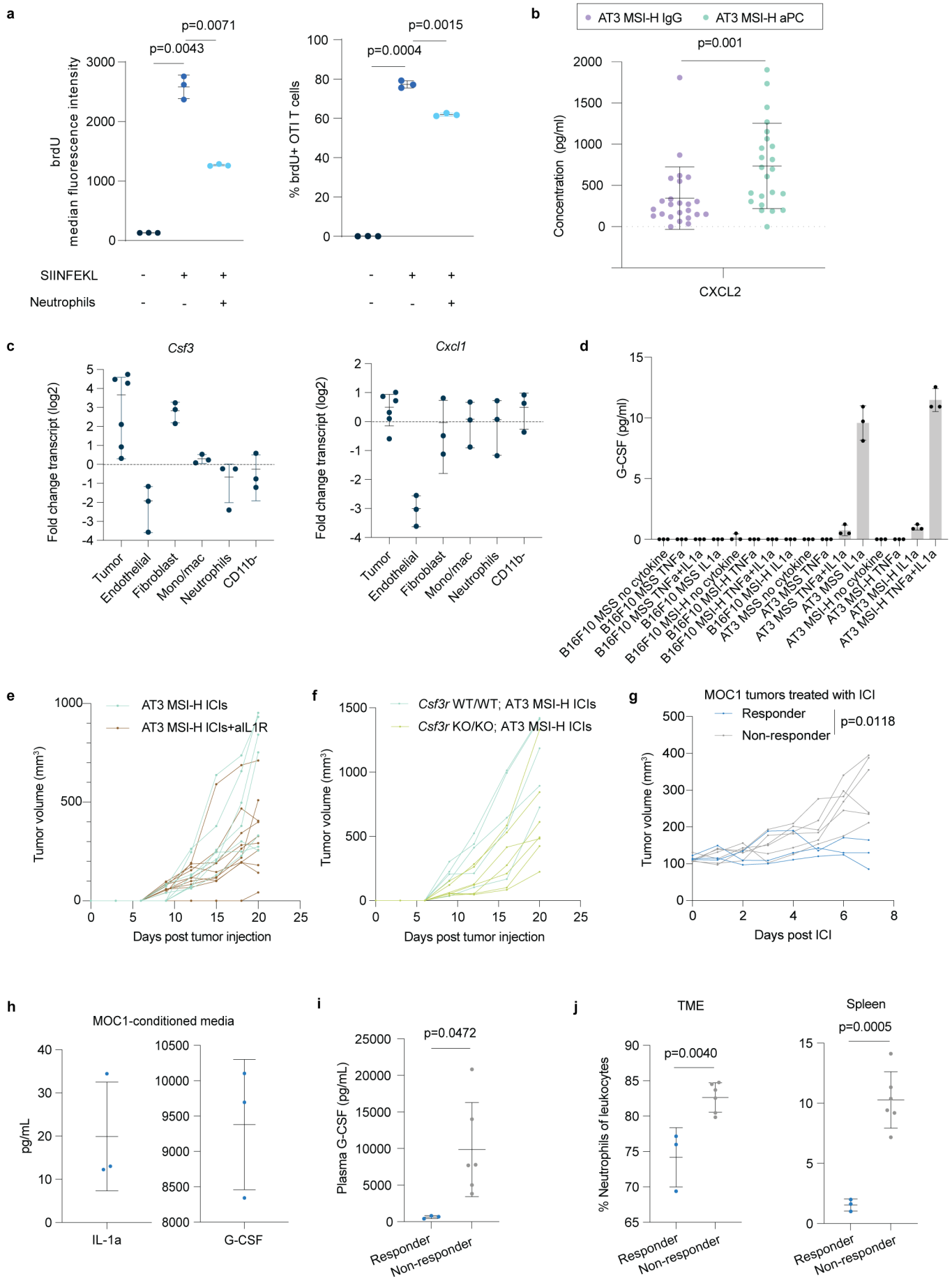

867

868 **Extended Data Fig. 3 ICI resistance is driven by G-CSF and PMN-MDSCs.**

869 **a,** brdU quantification for splenic OT-I T cells cultured with SIINFEKL peptide and/or sorted neutrophils from
870 AT3 MSI-H tumour. p values by t tests with Welch's correction and Holm-Sidak multiple testing correction.
871 center bar, mean. Upper and lower bars, SD. **b,** Quantification of CXCL2 in tumour lysates by multiplexed bead
872 assay. Two-tailed p values by Mann-Whitney test. **c,** Dot plot of experiment shown in Fig. 3f. **d,** Dot plot of
873 experiment shown in Fig 3g. **e,** Dot plot of individual mice of experiment shown in Fig. 3j. **f,** Dot plot of individual
874 mice of experiment shown in Fig. 3k. **g,** Tumour volume measurements for Moc1 tumour cells implanted in the
875 subcutaneous flank and treated with anti-PD-1 antibody, stratified by response to treatment. n = 3 and 6 mice
876 respectively for responder and non-responder groups. Two-tailed p values by t-test of day 7 post treatment tumour
877 volumes. **h,** Quantification of indicated cytokines by multiplexed bead assay from Moc1-conditioned cell culture
878 medium. **i,** Quantification of G-CSF by multiplexed bead assay from serum of Moc1 bearing mice, stratified by
879 treatment response. Two-tailed p values by t test. **j,** Quantification of neutrophils in the tumour and spleen of
880 responding and non-responding Moc1 bearing mice. Two-tailed p values by t test. Box plot: center line, median;
881 box limits, upper and lower quartiles; whiskers, 1.5x interquartile range. For all dot plots, center bar, mean. Upper
882 and lower bars, SD. For all tumour volume plots, center point = mean, upper and lower bars, SD.

Extended Data Fig. 4

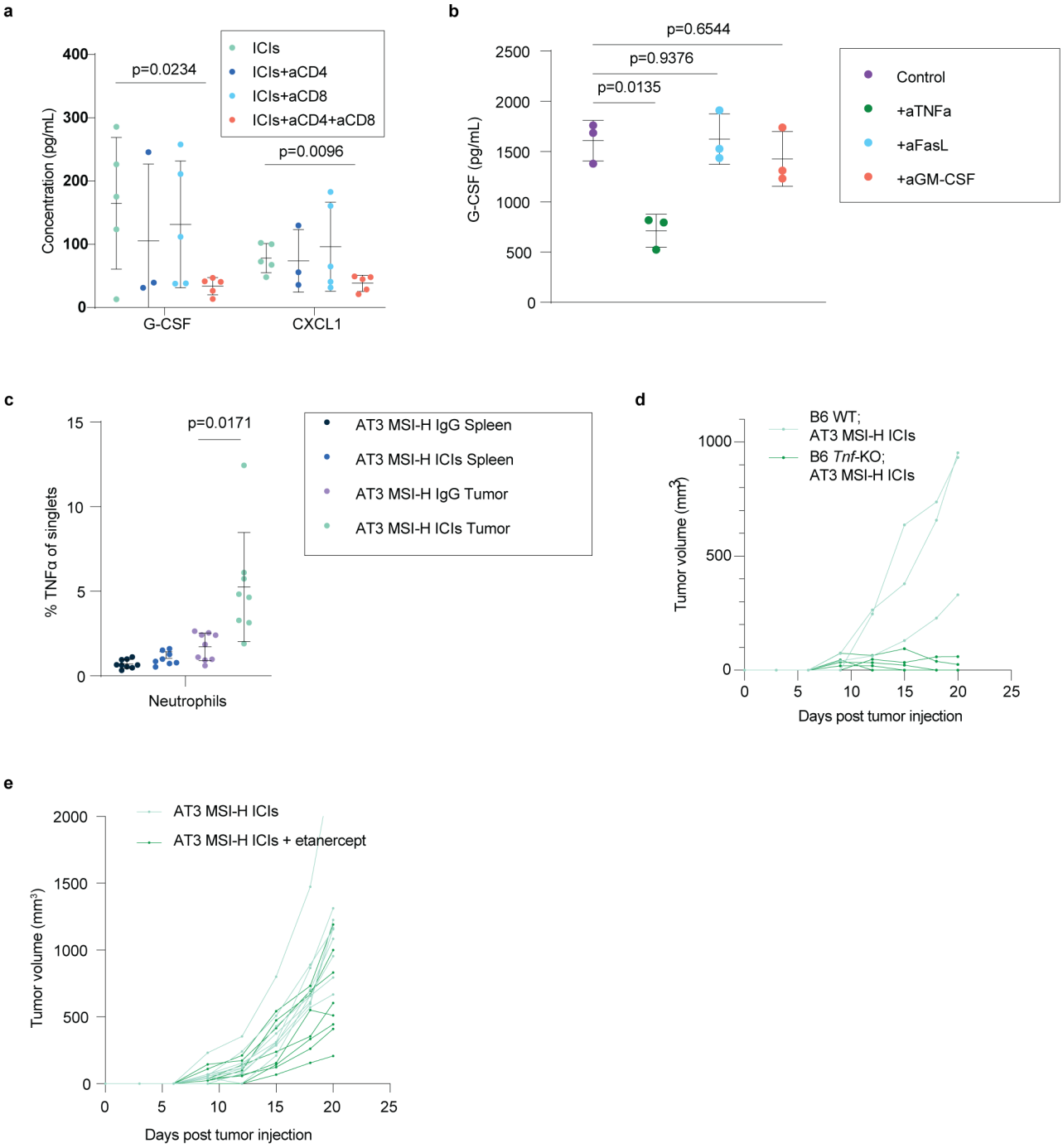

883

884 **Extended Data Fig. 4 Features of inflammatory cytokine production in the ICI resistant TME.**

885 **a,** Quantification of G-CSF and CXCL1 concentration from tumour lysates for AT3 MSI-H tumours treated with
886 the indicated antibodies. p values by two-tailed t test with Welch's correction and Holm-Sidak multiple testing
887 correction. **b,** Quantification of G-CSF concentration in supernatant of 24h culture containing indicated sorted
888 cell types from AT3 MSI-H tumours treated with ICIs, with or without addition of indicated neutralizing
889 antibodies. **c,** Quantification of TNFα+ neutrophils in tumour or spleen of AT3 MSI-H tumours treated with
890 indicated antibodies. p value by two-tailed t test with Welch's correction. **d,** Dot plot of individual mice for
891 experiment shown in Fig. 4g. **e,** Dot plot of individual mice for experiment shown in Fig. 4h. For all plots, center
892 bar, mean. Upper and lower bars, SD.

Extended Data Fig. 5

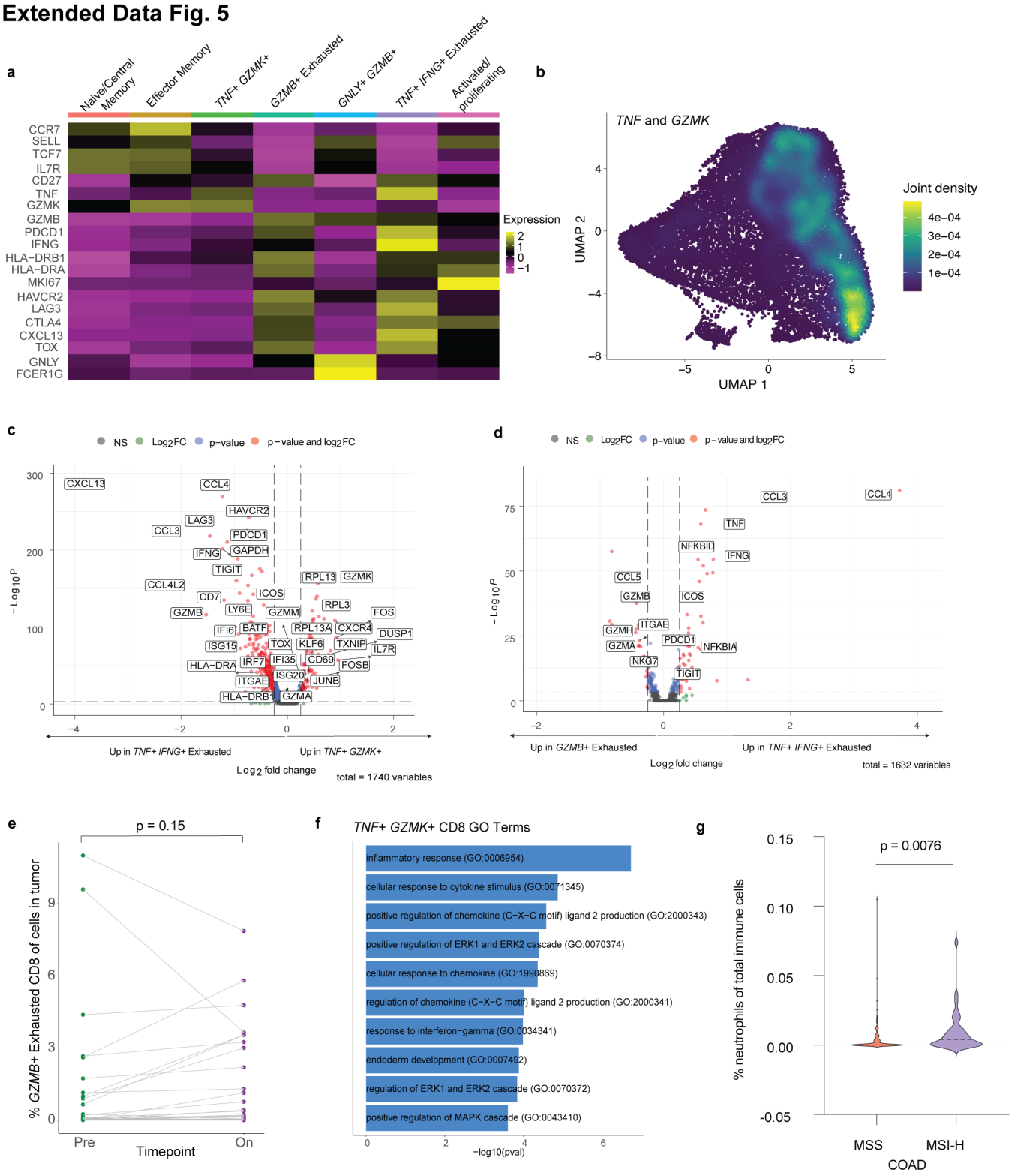

893

894 **Extended Data Fig. 5 ICI therapy-induced CD8 T cell, tumour, and neutrophil inflammation in human**

895 **cancer.**

896 **a,** Heatmap of genes defining CD8 T cell clusters. **b,** UMAP joint density plot of *TNF* and *GZMK*-expressing

897 CD8 T cells. **c,** Volcano plot of differential gene expression between *TNF*+ *IFNG*+ Exhausted CD8s and

898 *TNF*+*GZMK*+ CD8s. **d,** Volcano plot of differential gene expression between *GZMB*+ Exhausted CD8s and

899 *TNF*+ *IFNG*+ Exhausted CD8s. **e,** Percent of *GZMB*+ Exhausted CD8s out of all cells in tumour for Pre vs On

900 samples. Exact p value by two-tailed Wilcoxon matched-pairs signed rank test for paired samples are shown. **f,**

901 Gene Ontology (GO) terms enriched in *TNF*+*GZMK*+ CD8s. **g,** Violin plots of neutrophil quantification by

902 CIBERTSORTx from MSS and MSI-H COAD patients in TCGA.

Extended Data Fig. 6

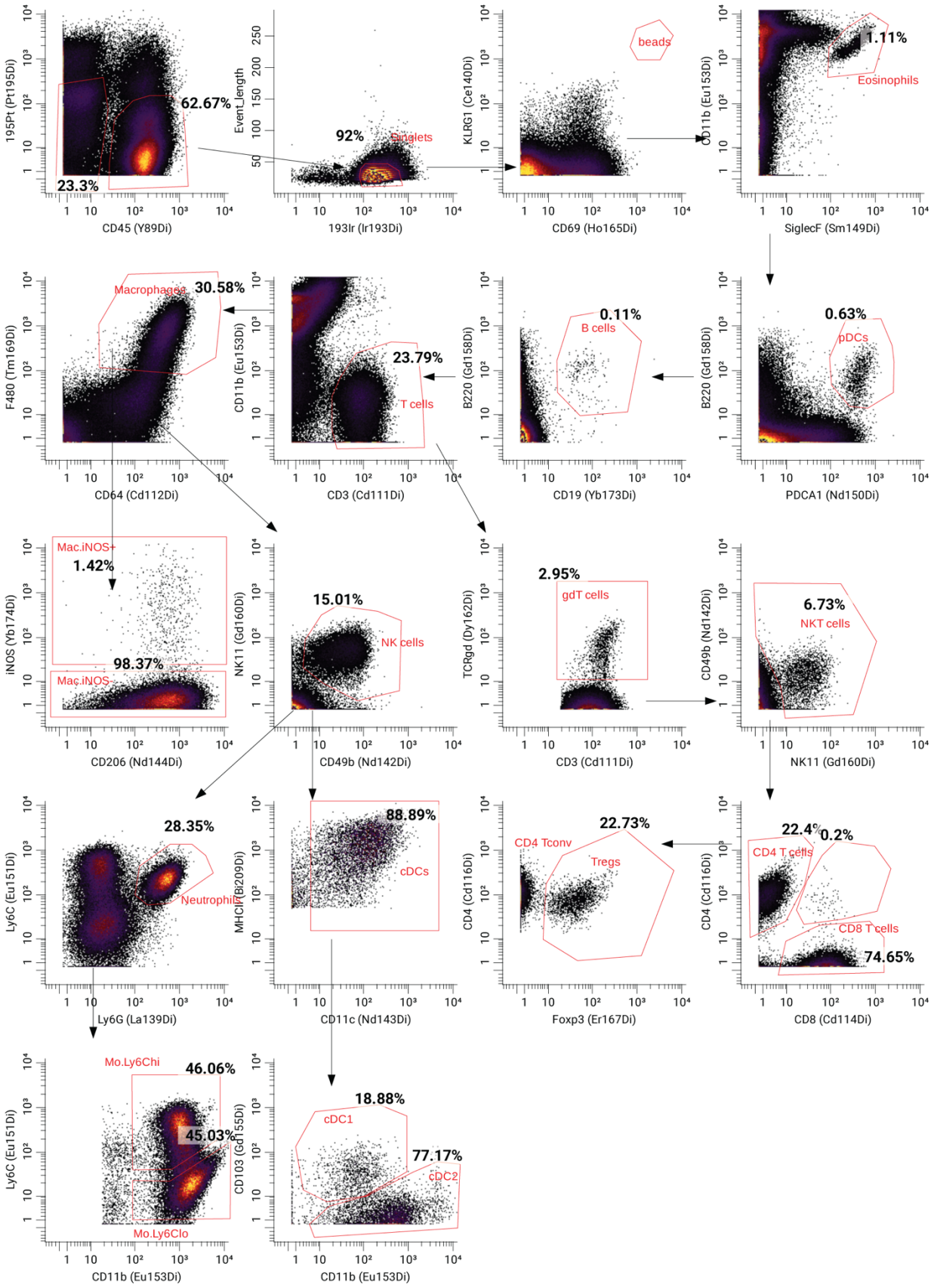

903

904 **Extended Data Fig. 6 Manual gating strategy for CyTOF dataset.**

905 Biaxial plots showing how each cell subpopulation was gated.

Extended Data Fig. 7

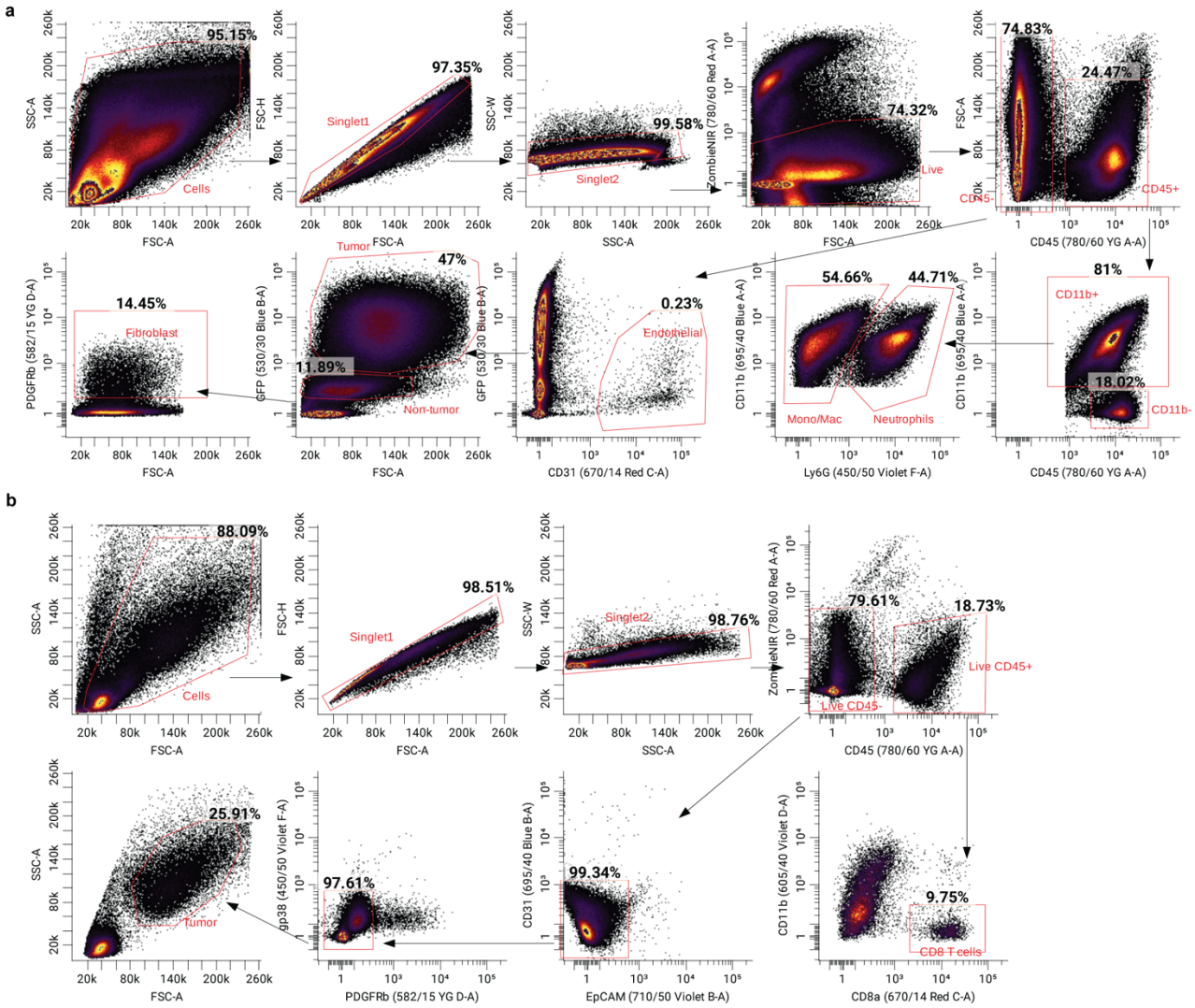

906

907 **Extended Data Fig. 7 Gating strategy for flow cytometry and cell sorting.**

908 **a,** Gating strategy used for experiment in Fig. 3f. **b,** Gating strategy used for CD8 T cell and tumour co-culture

909 experiments.

910 **Supplementary Table 1. CRISPR-Cas9 reagents and parameters**

911

Scrambled nontargeting control	GGTTCTTGACTACCGTAATT
AT3 MSH2 crRNA combination	GGTTAATACCCTGATACAGT + CACATGAGCGAAGCTAACAA
B16F10 MSH2 crRNA combination	CCTTAATAAATGCAGCCCGG + GGTTAATACCCTGATACAGT
EO771 MSH2 crRNA combination	GGTTAATACCCTGATACAGT + CACATGAGCGAAGCTAACAA
4T1 MSH2 crRNA combination	GGTTAATACCCTGATACAGT + CACATGAGCGAAGCTAACAA
ssODN	TTAGCTCTGTTTACGTCCCAGCGGGCATGAGAGTAACAAGAG GGTGTGGTAATATTACGGTACCGAGCACTATCGATACAATAT GTGTCATACGGACACG
AT3 buffer and code	Buffer SE, code DS-120
B16F10 buffer and code	Buffer SG, code DC-135
EO771 buffer and code	Buffer SE, code DS-120
4T1 buffer and code	Buffer SE, code DS-120

912

913 **Supplementary Table 2. Microsatellite instability analysis primer sequences**

914

AA003063 F	NED-ACGTCAAAAATCAATGTTAGG
AA003063 R	CAGCAAGGGTCCCTGTCTTA
AC096777 F	VIC- TCCCTGTATAACCCTGGCTGACT
AC096777 R	GCAACCAGTTGTCCTGGCGTGGA
L24372 F	FAM-GGGAAGACTGCTTAGGGAAGA
L24372 R	ATTTGGCTTTCAAGCATCCATA
U12235 F	VIC-GCTCATCTTCGTTCCCTGTC
U12235 R	CATTCGGTGGAAAGCTCTGA

915

916 **Supplementary Table 3. CyTOF antibody panel**
917

Channel	Metal	Protein	Titrated Conc. (ug/ml)	Clone	Isotype	Catalog	Vendor
89	Y	CD45	1.5	30-F11	rat IgG2b	103102	Biolegend
111	Cd	CD3	6	17A2	rat IgG2b	100202	Biolegend
112	Cd	CD64	6	X54--5/7.1	mouse IgG1	139302	Biolegend
113	In	Ter119	3	TER-119	Rat IgG2b	116202	Biolegend
114	Cd	CD8	3	53-6.7	rat IgG2a	100702	Biolegend
116	Cd	CD4	1.5	RM-5	rat IgG2a	100506	Biolegend
139	La	Ly6G	0.375	1A8	rat IgG2a	127626	Biolegend
140	Ce	KLRG1	1.5	2F1	syrian hamster IgG2	562190	BD biosciences
141	Pr	granzyme B	3	QA16A02	mouse IgG1	372202	Biolegend
142	Nd	CD49b	0.75	HMa2	armenian hamster IgG	103501	Biolegend
143	Nd	CD11c	0.75	N418	armenian hamster IgG	117341	Biolegend
144	Nd	CD206	0.75	C068C2	rat IgG2a	141702	Biolegend
145	Nd	CD27	6	LG 3A10	armenian hamster IgG	124202	Biolegend
146	Nd	CD138	6	281-2	rat IgG2a	142502	Biolegend
147	Sm	PD-L1	3	10F.9G2	rat IgG2b	124302	Biolegend
148	Nd	ICOS	3	C398.4A	armenian hamster IgG	313502	Biolegend
149	Sm	SiglecF	1.5	E50-2440	rat IgG2a	552125	BD biosciences
150	Nd	PDCA-1	0.75	120G8.04	rat IgG1	DDX0390P-100	Novus Biologicals
151	Eu	Ly6C	0.375	HK1.4	rat IgG2c	128002	Biolegend
152	Sm	Ki67	1.5	SolA15	rat IgG2a	14-5698-82	Thermo Fisher
153	Eu	CD11b	1.5	HK1.4	rat IgG2b	101202	Biolegend
154	Sm	cKit	1.5	2B8	rat IgG2b	105802	Biolegend
155	Gd	CD103	1.5	2E7	armenian hamster IgG	121402	Biolegend
156	Gd	CD80	0.1875	16-10A1	armenian hamster IgG	104702	Biolegend
157	Gd	CD83	1.5	Michel-19	rat IgG1	121502	Biolegend
158	Gd	B220	1.5	RA3-6B2	rat IgG2a	103202	Biolegend
159	Tb	PD-1	0.375	29F.1A12	rat IgG2a	135202	Biolegend
160	Gd	NK1.1	1.5	PK136	mouse IgG2a	108702	Biolegend
161	Dy	T-bet	6	4B10	mouse IgG1	644825	Biolegend
162	Dy	TCRgd	0.75	GL3	armenian hamster IgG	118101	Biolegend

163	Dy	CD62L	6	95218	rat IgG2a	MAB5761	R&D Systems
164	Dy	TCF1	1.5	2203	rabbit IgG	2203S	Cell Signaling
165	Ho	CD69	3	H1.2F3	armenian hamster IgG	104502	Biolegend
166	Er	FcER1a	3	MAR-1	armenian hamster IgG	134321	Biolegend
167	Er	Foxp3	3	NRRF-30	rat IgG2a	14-4771-80	Thermo Fisher
168	Er	CD86	0.1875	GL-1	rat IgG2a	105002	Biolegend
169	Tm	F4/80	6	BM8	rat IgG2a	123143	Biolegend
170	Er	CD115	1.5	AFS98	rat IgG2a	135521	Biolegend
171	Yb	CD38	0.75	90	rat IgG2a	102723	Biolegend
172	Yb	TIM3	3	RMT3-23	rat IgG2a	119702	Biolegend
173	Yb	CD19	0.375	6D5	rat IgG2a	115547	Biolegend
174	Yb	iNOS	0.75	CXNFT	rat IgG2a	14-5920-82	Thermo Fisher
175	Lu	CD44	0.375	IM7	rat IgG2b	103002	Biolegend
176	Yb	CD39	0.75	24DMS1	rat IgG2b	14-0391-82	Thermo Fisher
209	Bi	MHC II	0.1	M5/114.15.2	rat IgG2b	107602	Biolegend

919 **Supplementary Table 4. Flow cytometry antibodies**
920

Target	Fluorophore	Vendor	Clone	Catalog
BrdU	APC	Thermo Fisher		8817-6600-42
CD11b	BV711	Biolegend	M1/70	101241
CD11b	PerCP-Cy5.5	Biolegend	M1/70	101228
CD31	APC	Biolegend	390	102410
CD31	PerCP-Cy5.5	Biolegend	390	102420
CD4	BV510	Biolegend	RM4-5	100559
CD45	PE-Cy7	Biolegend	30-F11	103114
CD45.1	PE	Biolegend	A20	110708
CD8a	APC	Biolegend	53-6.7	100712
CD8a	BV650	Biolegend	53-6.7	100741
CD8a	PerCP-Cy5.5	Biolegend	53-6.7	100734
EpCAM	BV605	Biolegend	G8.8	118227
F4/80	PerCP-Cy5.5	Biolegend	BM8	123127
gp38	BV421	Biolegend	8.1.1	127423
H-2Kb/H-2Db	FITC	Biolegend	28-8-6	114605
IkBa	AF488	Cell Signaling Technology	93H1	4886S
Ly6G	BV421	Biolegend	1A8	127627
Ly6G	PE-Cy7	Biolegend	1A8	127618
NK1.1	PE	BD Biosciences	PK136	553165
PDGFRb	PE	Biolegend	APB5	136006
TCRb	BV421	Biolegend	H57-597	109230
TNFa	APC	Biolegend	MP6-XT22	506308

921

Supplementary Table 5. Test statistics

Fig. 1d

	P value	Mean rank of Column A	Mean rank of Column B	Mean rank diff.	Mann-Whitney U	Adjusted P Value
MSS IgG vs MSI-H IgG	0.2814	17.87	14.25	3.617	92.00	0.2814
MSS ICIs vs MSI-H ICIs	0.0037	22.20	12.67	9.533	57.00	0.0074
MSS IgG vs MSS ICIs	0.0003	21.07	9.933	11.13	29.00	0.0008
MSI-H IgG vs MSI-H ICIs	<0.0001	24.81	11.00	13.81	27.00	<0.0001

Fig. 1e

	P value	Mean rank of Column A	Mean rank of Column B	Mean rank diff.	Mann-Whitney U	Adjusted P Value
MSS IgG vs MSI-H IgG	0.5116	10.09	12.00	-1.909	45.00	0.8835
MSS ICIs vs MSI-H ICIs	0.3000	10.00	13.00	-3.000	44.00	0.7599
MSS IgG vs MSS ICIs	0.8470	11.18	11.82	-0.6364	57.00	0.9766
MSI-H IgG vs MSI-H ICIs	0.9725	11.10	10.91	0.1909	54.00	0.9766

Extended Data Fig. 1e

Column B	B16F10 MSI-H
vs.	vs.
Column A	B16F10 MSS
Unpaired t test	
P value	0.5578
P value summary	ns
Significantly different (P < 0.05)?	No
One- or two-tailed P value?	Two-tailed
t, df	t=0.6386, df=4
How big is the difference?	
Mean of column A	16.89
Mean of column B	16.21
Difference between means (B - A) ± SEM	-0.6733 ± 1.054
95% confidence interval	-3.601 to 2.254
R squared (eta squared)	0.09253
F test to compare variances	
F, DFn, Dfd	83.57, 2, 2
P value	0.0236
P value summary	*
Significantly different (P < 0.05)?	Yes
Data analyzed	
Sample size, column A	3
Sample size, column B	3

Column B	AT3 MSI-H
vs.	vs.
Column A	AT3 MSS
Unpaired t test	
P value	0.8465

P value summary	ns
Significantly different (P < 0.05)?	No
One- or two-tailed P value?	Two-tailed
t, df	t=0.2065, df=4
How big is the difference?	
Mean of column A	13.07
Mean of column B	13.00
Difference between means (B - A) ± SEM	-0.06667 ± 0.3228
95% confidence interval	-0.9630 to 0.8296
R squared (eta squared)	0.01055
F test to compare variances	
F, DFn, Dfd	7.009, 2, 2
P value	0.2497
P value summary	ns
Significantly different (P < 0.05)?	No
Data analyzed	
Sample size, column A	3
Sample size, column B	3

Column B	4T1 MSI-H
vs.	vs.
Column A	4T1 MSS
Unpaired t test	
P value	0.1254
P value summary	ns
Significantly different (P < 0.05)?	No
One- or two-tailed P value?	Two-tailed
t, df	t=1.933, df=4
How big is the difference?	
Mean of column A	14.70
Mean of column B	13.98
Difference between means (B - A) ± SEM	-0.7167 ± 0.3708
95% confidence interval	-1.746 to 0.3128
R squared (eta squared)	0.4829
F test to compare variances	
F, DFn, Dfd	9.011, 2, 2
P value	0.1998
P value summary	ns
Significantly different (P < 0.05)?	No
Data analyzed	
Sample size, column A	3
Sample size, column B	3

Fig. 2b

Column B	AT3 MSI-H ICIs
vs.	vs.
Column A	AT3 MSI-H IgG
Unpaired t test with Welch's correction	
P value	0.0303
P value summary	*

Significantly different (P < 0.05)?	Yes
One- or two-tailed P value?	Two-tailed
Welch-corrected t, df	t=2.563, df=9.086
How big is the difference?	
Mean of column A	3.086
Mean of column B	5.384
Difference between means (B - A) ± SEM	2.299 ± 0.8969
95% confidence interval	0.2727 to 4.325
R squared (eta squared)	0.4196
F test to compare variances	
F, DFn, Dfd	13.25, 8, 9
P value	0.0008
P value summary	***
Significantly different (P < 0.05)?	Yes
Data analyzed	
Sample size, column A	10
Sample size, column B	9

Fig. 2i

	P value	Mean of Column A	Mean of Column B	Difference	SE of difference	t ratio	df	Adjusted P Value
B16F10 MSI-H IgG vs B16F10 MSI-H ICIs	0.0014	68.96	84.62	-15.66	4.135	3.787	18.00	0.0027
AT3 MSI-H IgG vs AT3 MSI-H ICIs	0.2925	37.71	33.76	3.948	3.634	1.086	17.00	0.2925
B16F10 MSI-H ICIs vs AT3 MSI-H ICIs	<0.0001	84.62	33.76	50.86	4.134	12.30	17.00	<0.0001

Extended Data Fig. 2a

Table Analyzed	e63 data
Kruskal-Wallis test	
P value	<0.0001
Exact or approximate P value?	Approximate
P value summary	****
Do the medians vary signif. (P < 0.05)?	Yes
Number of groups	8
Kruskal-Wallis statistic	49.16
Data summary	
Number of treatments (columns)	8
Number of values (total)	69

Extended Data Fig. 2f

	P value	Mean rank of Column A	Mean rank of Column B	Mean rank diff.	Mann-Whitney U	Adjusted P Value
B16F10 MSI-H IgG vs B16F10 MSI-H ICIs	<0.0001	5.600	15.40	-9.800	1.000	<0.0001
AT3 MSI-H IgG vs AT3 MSI-H ICIs	0.0947	7.900	12.33	-4.433	24.00	0.0947

938
939 **Extended Data Fig. 2g**

	P value	Mean rank of Column A	Mean rank of Column B	Mean rank diff.	Mann-Whitney U	Adjusted P Value
B16F10 MSI-H IgG vs B16F10 MSI-H ICIs	<0.0001	5.500	15.50	-10.00	0.000	<0.0001
AT3 MSI-H IgG vs AT3 MSI-H ICIs	0.0076	6.800	13.56	-6.756	13.00	0.0076
B16F10 MSI-H ICIs vs AT3 MSI-H ICIs	<0.0001	14.50	5.000	9.500	0.000	<0.0001

940
941 **Fig. 3a**

	P value	Mean of Column A	Mean of Column B	Difference	SE of difference	t ratio	df	Adjusted P Value
B16F10 MSI-H ICIs vs AT3 MSI-H ICIs	0.0012	0.4607	16.31	-15.85	3.233	4.901	8.013	0.0024
AT3 MSI-H IgG vs AT3 MSI-H ICIs	0.0377	8.085	16.31	-8.221	3.440	2.390	10.11	0.0377

942
943 **Fig. 3e**

Table Analyzed	G-CSF
Column B	AT3 MSI-H ICIs
vs.	vs.
Column A	AT3 MSI-H IgG
Mann Whitney test	
P value	0.0001
Exact or approximate P value?	Exact
P value summary	***
Significantly different (P < 0.05)?	Yes
One- or two-tailed P value?	Two-tailed
Sum of ranks in column A,B	404 , 724
Mann-Whitney U	104
Difference between medians	
Median of column A	73.35, n=24
Median of column B	233.2, n=23
Difference: Actual	159.8
Difference: Hodges-Lehmann	148.5

944

Table Analyzed	CXCL1
Column B	AT3 MSI-H ICIs
vs.	vs.
Column A	AT3 MSI-H IgG
Mann Whitney test	
P value	0.0015
Exact or approximate P value?	Exact
P value summary	**
Significantly different (P < 0.05)?	Yes
One- or two-tailed P value?	Two-tailed

Sum of ranks in column A,B	430 , 698
Mann-Whitney U	130
Difference between medians	
Median of column A	77.79, n=24
Median of column B	213.8, n=23
Difference: Actual	136.0
Difference: Hodges-Lehmann	102.6

Fig. 3h

Column B	AT3 MSI-H
vs.	vs.
Column A	B16F10 MSI-H
Unpaired t test	
P value	<0.0001
P value summary	****
Significantly different (P < 0.05)?	Yes
One- or two-tailed P value?	Two-tailed
t, df	t=37.25, df=4
How big is the difference?	
Mean of column A	-10.46
Mean of column B	-47.65
Difference between means (B - A) ± SEM	-37.19 ± 0.9982
95% confidence interval	-39.96 to -34.42
R squared (eta squared)	0.9971
F test to compare variances	
F, DFn, Dfd	5.776, 2, 2
P value	0.2952
P value summary	ns
Significantly different (P < 0.05)?	No
Data analyzed	
Sample size, column A	3
Sample size, column B	3

Fig. 3i

Table Analyzed	G-CSF
Column B	AT3 MSI-H ICIs + aIL1R
vs.	vs.
Column A	AT3 MSI-H ICIs
Mann Whitney test	
P value	0.0286
Exact or approximate P value?	Exact
P value summary	*
Significantly different (P < 0.05)?	Yes
One- or two-tailed P value?	One-tailed
Sum of ranks in column A,B	18 , 10
Mann-Whitney U	0
Difference between medians	
Median of column A	225.9, n=3
Median of column B	13.03, n=4
Difference: Actual	-212.9
Difference: Hodges-Lehmann	-212.9

Table Analyzed	CXCL1
Column B	AT3 MSI-H ICIs + aIL1R
vs.	vs.
Column A	AT3 MSI-H ICIs
Mann Whitney test	
P value	0.0571
Exact or approximate P value?	Exact
P value summary	ns
Significantly different (P < 0.05)?	No
One- or two-tailed P value?	One-tailed
Sum of ranks in column A,B	17 , 11
Mann-Whitney U	1
Difference between medians	
Median of column A	162.3, n=3
Median of column B	35.88, n=4
Difference: Actual	-126.4
Difference: Hodges-Lehmann	-126.4

Fig. 3j

Column B	AT3 MSI-H ICIs+aIL1R
vs.	vs.
Column A	AT3 MSI-H ICIs
Unpaired t test	
P value	0.0318
P value summary	*
Significantly different (P < 0.05)?	Yes
One- or two-tailed P value?	Two-tailed
t, df	t=2.367, df=15
How big is the difference?	
Mean of column A	619.9
Mean of column B	326.9
Difference between means (B - A) ± SEM	-293.0 ± 123.8
95% confidence interval	-556.9 to -29.12
R squared (eta squared)	0.2719
F test to compare variances	
F, DFn, Dfd	2.737, 6, 9
P value	0.1695
P value summary	ns
Significantly different (P < 0.05)?	No
Data analyzed	
Sample size, column A	7
Sample size, column B	10

Fig. 3f

Column B	GCSFR WT/WT
vs.	vs.
Column A	GCSFR KO/KO
Unpaired t test	
P value	0.0323
P value summary	*

Significantly different (P < 0.05)?	Yes
One- or two-tailed P value?	Two-tailed
t, df	t=2.484, df=10
How big is the difference?	
Mean of column A	629.5
Mean of column B	1127
Difference between means (B - A) ± SEM	497.5 ± 200.3
95% confidence interval	51.20 to 943.7
R squared (eta squared)	0.3815
F test to compare variances	
F, DFn, Dfd	1.348, 6, 4
P value	0.8061
P value summary	ns
Significantly different (P < 0.05)?	No
Data analyzed	
Sample size, column A	7
Sample size, column B	5

Extended Data Fig. 3a

BrdU MFI	P value	Mean of Column A	Mean of Column B	Difference	SE of difference	t ratio	df	Adjusted P Value
Negative control vs positive control	0.0022	129.4	2583	-2454	114.0	21.52	2.000	0.0043
Positive control vs +neutrophils	0.0071	2583	1266	1317	114.5	11.50	2.030	0.0071

% brdU+ OT1 T cells	P value	Mean of Column A	Mean of Column B	Difference	SE of difference	t ratio	df	Adjusted P Value
Negative control vs positive control	0.0002	0.04386	77.32	-77.28	1.062	72.74	2.007	0.0004
Positive control vs +neutrophils	0.0015	77.32	61.87	15.45	1.156	13.37	2.716	0.0015

Extended Data Fig. 3b

Table Analyzed	CXCL2
Column B	AT3 MSI-H ICIs
vs.	vs.
Column A	AT3 MSI-H IgG
Mann Whitney test	
P value	0.0010
Exact or approximate P value?	Exact
P value summary	**
Significantly different (P < 0.05)?	Yes
One- or two-tailed P value?	Two-tailed
Sum of ranks in column A,B	425.5 , 702.5
Mann-Whitney U	125.5
Difference between medians	
Median of column A	240.8, n=24
Median of column B	697.9, n=23
Difference: Actual	457.0
Difference: Hodges-Lehmann	333.9

Extended Data Fig. 3g

Table Analyzed	Day 7 tumor sizes
Column B	Non-responder
vs.	vs.
Column A	Responder
Unpaired t test	
P value	0.0118
P value summary	*
Significantly different (P < 0.05)?	Yes
One- or two-tailed P value?	Two-tailed
t, df	t=3.379, df=7
How big is the difference?	
Mean of column A	126.5
Mean of column B	303.9
Difference between means (B - A) ± SEM	177.4 ± 52.48
95% confidence interval	53.25 to 301.5
R squared (eta squared)	0.6199
F test to compare variances	
F, DFn, Dfd	4.500, 5, 2
P value	0.3835
P value summary	ns
Significantly different (P < 0.05)?	No
Data analyzed	
Sample size, column A	3
Sample size, column B	6

Extended Data Fig. 3i

Table Analyzed	G-CSF responder vs non-responder
Column B	Non-responder
vs.	vs.
Column A	Responder
Unpaired t test	
P value	0.0472
P value summary	*
Significantly different (P < 0.05)?	Yes
One- or two-tailed P value?	Two-tailed
t, df	t=2.404, df=7
How big is the difference?	
Mean of column A	629.3
Mean of column B	9859
Difference between means (B - A) ± SEM	9230 ± 3839
95% confidence interval	152.5 to 18307
R squared (eta squared)	0.4523
F test to compare variances	
F, DFn, Dfd	1076, 5, 2
P value	0.0019
P value summary	**
Significantly different (P < 0.05)?	Yes
Data analyzed	
Sample size, column A	3
Sample size, column B	6

Extended Data Fig. 3j

Table Analyzed	TME % Neutrophils of leukocytes
Column B	Non-responder
vs.	vs.
Column A	Responder
Unpaired t test	
P value	0.0040
P value summary	**
Significantly different (P < 0.05)?	Yes
One- or two-tailed P value?	Two-tailed
t, df	t=4.202, df=7
How big is the difference?	
Mean of column A	74.18
Mean of column B	82.64
Difference between means (B - A) ± SEM	8.462 ± 2.014
95% confidence interval	3.700 to 13.22
R squared (eta squared)	0.7161
F test to compare variances	
F, DFn, Dfd	4.024, 2, 5
P value	0.1818
P value summary	ns
Significantly different (P < 0.05)?	No
Data analyzed	
Sample size, column A	3
Sample size, column B	6

Table Analyzed	Spleen % Neutrophils of leukocytes
Column B	Non-responder
vs.	vs.
Column A	Responder
Unpaired t test	
P value	0.0005
P value summary	***
Significantly different (P < 0.05)?	Yes
One- or two-tailed P value?	Two-tailed
t, df	t=6.177, df=7
How big is the difference?	
Mean of column A	1.540
Mean of column B	10.27
Difference between means (B - A) ± SEM	8.729 ± 1.413
95% confidence interval	5.387 to 12.07
R squared (eta squared)	0.8450
F test to compare variances	
F, DFn, Dfd	21.64, 5, 2
P value	0.0895
P value summary	ns
Significantly different (P < 0.05)?	No
Data analyzed	
Sample size, column A	3
Sample size, column B	6

967 **Fig. 4a**

	P value	Mean rank of Column A	Mean rank of Column B	Mean rank diff.	Mann-Whitney U	Adjusted P Value
MSS earl vys MSS late	0.7209	8.000	9.000	-1.000	28.00	0.7209
MMRd early vs MMRd late	0.0281	5.875	11.13	-5.250	11.00	0.0555

968

969 **Fig. 4b**

Table Analyzed	GCSF
Column B	AT3 MSI-H aThy1+ICIs
vs.	vs.
Column A	AT3 MSI-H ICIs
Unpaired t test with Welch's correction	
P value	0.0426
P value summary	*
Significantly different (P < 0.05)?	Yes
One- or two-tailed P value?	Two-tailed
Welch-corrected t, df	t=3.381, df=3.023
How big is the difference?	
Mean of column A	558.0
Mean of column B	38.09
Difference between means (B - A) ± SEM	-519.9 ± 153.8
95% confidence interval	-1007 to -32.63
R squared (eta squared)	0.7908
F test to compare variances	
F, DFn, Dfd	204.9, 3, 4
P value	0.0002
P value summary	***
Significantly different (P < 0.05)?	Yes
Data analyzed	
Sample size, column A	4
Sample size, column B	5

970

971 **Fig. 4c**

Table Analyzed	CXCL1
Column B	AT3 MSI-H aThy1+ICIs
vs.	vs.
Column A	AT3 MSI-H ICIs
Unpaired t test with Welch's correction	
P value	0.0438
P value summary	*
Significantly different (P < 0.05)?	Yes
One- or two-tailed P value?	Two-tailed
Welch-corrected t, df	t=3.258, df=3.163
How big is the difference?	
Mean of column A	280.5
Mean of column B	80.59
Difference between means (B - A) ± SEM	-200.0 ± 61.37
95% confidence interval	-389.7 to -10.22
R squared (eta squared)	0.7704
F test to compare variances	
F, DFn, Dfd	29.49, 3, 4

P value	0.0069
P value summary	**
Significantly different (P < 0.05)?	Yes
Data analyzed	
Sample size, column A	4
Sample size, column B	5

Fig. 4d

Table Analyzed	Neutrophils percent of singlets
Column B	AT3 MSI-H ICI + aThy1
vs.	vs.
Column A	AT3 MSI-H ICIs
Mann Whitney test	
P value	0.0635
Exact or approximate P value?	Exact
P value summary	ns
Significantly different (P < 0.05)?	No
One- or two-tailed P value?	Two-tailed
Sum of ranks in column A,B	28 , 17
Mann-Whitney U	2
Difference between medians	
Median of column A	16.53, n=4
Median of column B	6.103, n=5
Difference: Actual	-10.42
Difference: Hodges-Lehmann	-9.135

Fig. 4e

	P value	Mean of Column A	Mean of Column B	Difference	SE of difference	t ratio	df	Adjusted P Value
Tumor vs CD8+Tumor	0.0170	66.41	498.7	-432.3	63.65	6.792	2.166	0.0337
CD8+Tumor vs CD8+Tumor+aTNFa	0.0192	498.7	188.7	310.0	74.62	4.154	3.455	0.0337

Fig. 4f

Table Analyzed	% TNFa+ of singlets CD4
Column B	AT3 MSI-H ICIs Tumor
vs.	vs.
Column A	AT3 MSI-H IgG Tumor
Unpaired t test	
P value	0.0043
P value summary	**
Significantly different (P < 0.05)?	Yes
One- or two-tailed P value?	Two-tailed
t, df	t=4.158, df=7
How big is the difference?	
Mean of column A	0.1284
Mean of column B	0.3553
Difference between means (B - A) ± SEM	0.2269 ± 0.05457
95% confidence interval	0.09787 to 0.3559
R squared (eta squared)	0.7118
F test to compare variances	
F, DFn, Dfd	5.776, 3, 4

P value	0.1233
P value summary	ns
Significantly different (P < 0.05)?	No
Data analyzed	
Sample size, column A	5
Sample size, column B	4

977

Table Analyzed	% TNFa+ of singlets CD8
Column B	AT3 MSI-H ICIs Tumor
vs.	vs.
Column A	AT3 MSI-H IgG Tumor
Unpaired t test	
P value	0.0318
P value summary	*
Significantly different (P < 0.05)?	Yes
One- or two-tailed P value?	Two-tailed
t, df	t=2.674, df=7
How big is the difference?	
Mean of column A	0.2564
Mean of column B	0.4595
Difference between means (B - A) ± SEM	0.2030 ± 0.07593
95% confidence interval	0.02349 to 0.3826
R squared (eta squared)	0.5053
F test to compare variances	
F, DFn, Dfd	3.826, 3, 4
P value	0.2277
P value summary	ns
Significantly different (P < 0.05)?	No
Data analyzed	
Sample size, column A	5
Sample size, column B	4

978

979 **Fig. 4g**

Table Analyzed	
Column C	AT3 MSI-H ICIs B6TNFko
vs.	vs.
Column B	AT3 MSI-H ICIs B6WT
Mann Whitney test	
P value	0.0357
Exact or approximate P value?	Exact
P value summary	*
Significantly different (P < 0.05)?	Yes
One- or two-tailed P value?	Two-tailed
Sum of ranks in column B,C	21 , 15
Mann-Whitney U	0
Difference between medians	
Median of column B	932.6, n=3
Median of column C	0.000, n=5
Difference: Actual	-932.6
Difference: Hodges-Lehmann	-907.3

980

Fig. 4h

Column B	ICIs+etanercept
vs.	vs.
Column A	ICIs
Mann Whitney test	
P value	0.0152
Exact or approximate P value?	Exact
P value summary	*
Significantly different (P < 0.05)?	Yes
One- or two-tailed P value?	Two-tailed
Sum of ranks in column A,B	106 , 47
Mann-Whitney U	11
Difference between medians	
Median of column A	1156, n=9
Median of column B	556.9, n=8
Difference: Actual	-599.0
Difference: Hodges-Lehmann	-495.8

Extended Data Fig. 4a

Table Analyzed	G-CSF
Column D	aCD4CD8+ICIs
vs.	vs.
Column A	ICIs
Unpaired t test	
P value	0.0234
P value summary	*
Significantly different (P < 0.05)?	Yes
One- or two-tailed P value?	Two-tailed
t, df	t=2.793, df=8
How big is the difference?	
Mean of column A	164.7
Mean of column D	33.69
Difference between means (D - A) ± SEM	-131.0 ± 46.90
95% confidence interval	-239.2 to -22.86
R squared (eta squared)	0.4938
F test to compare variances	
F, DFn, Dfd	58.28, 4, 4
P value	0.0017
P value summary	**
Significantly different (P < 0.05)?	Yes
Data analyzed	
Sample size, column A	5
Sample size, column D	5

Table Analyzed	CXCL1
Column D	aCD4CD8+ICIs
vs.	vs.
Column A	ICIs
Unpaired t test	
P value	0.0096
P value summary	**

Significantly different (P < 0.05)?	Yes
One- or two-tailed P value?	Two-tailed
t, df	t=3.380, df=8
How big is the difference?	
Mean of column A	78.02
Mean of column D	38.28
Difference between means (D - A) ± SEM	-39.74 ± 11.76
95% confidence interval	-66.84 to -12.63
R squared (eta squared)	0.5882
F test to compare variances	
F, DFn, Dfd	3.233, 4, 4
P value	0.2822
P value summary	ns
Significantly different (P < 0.05)?	No
Data analyzed	
Sample size, column A	5
Sample size, column D	5

Extended Data Fig. 4b

	P value	Mean of Column A	Mean of Column B	Difference	SE of difference	t ratio	df	Adjusted P Value
Control vs aTNFa	0.0045	1609	711.9	897.3	150.4	5.967	3.832	0.0135
Control vs aFasL	0.9376	1609	1625	-15.58	186.5	0.08353	3.825	0.9376
Control vs aGMCSF	0.4121	1609	1428	181.5	196.5	0.9236	3.687	0.6544

Extended Data Fig. 4c

Table Analyzed	% TNFa+ of singlets neutrophils
Column B	AT3 MSI-H ICIs Tumor
vs.	vs.
Column A	AT3 MSI-H IgG Tumor
Unpaired t test with Welch's correction	
P value	0.0171
P value summary	*
Significantly different (P < 0.05)?	Yes
One- or two-tailed P value?	Two-tailed
Welch-corrected t, df	t=3.019, df=7.790
How big is the difference?	
Mean of column A	1.721
Mean of column B	5.261
Difference between means (B - A) ± SEM	3.540 ± 1.172
95% confidence interval	0.8235 to 6.256
R squared (eta squared)	0.5392
F test to compare variances	
F, DFn, Dfd	15.76, 7, 8
P value	0.0009
P value summary	***
Significantly different (P < 0.05)?	Yes
Data analyzed	
Sample size, column A	9
Sample size, column B	8

990 **Fig. 5e**

Table Analyzed	TNKF+GZMK+ CD8 frequency
Column B	Pre
vs	vs
Column A	On
Wilcoxon signed rank sum	
P value	0.000607
Exact or approximate P value?	exact
P value summary	***
Significantly different (P<0.05)?	Yes
One- or two-tailed P value?	Two-tailed
V statistic	369
Lower 95% CI	0.57093
Upper 95% CI	2.655315

991

992 **Fig. 5f**

Table Analyzed	Correlation of TNF+GZMK+ and TU NFkB score
Column B	Change in frequency of TNF+GZMK+
vs	vs
Column A	Change in TU NFkB/TNF score
Spearman Correlation	
P value	0.039
Exact or approximate P value?	exact
P value summary	*
Significantly different (P<0.05)?	Yes
rho value	0.39

993

994 **Fig. 5g**

Table Analyzed	Correlation of GZMB+Exhausted and TU NFkB score
Column B	Change in frequency of GZMB+Exhausted
vs	vs
Column A	Change in TU NFkB/TNF score
Spearman Correlation	
P value	0.47
Exact or approximate P value?	exact
P value summary	n.s.
Significantly different (P<0.05)?	No
rho value	0.14

995

996 **Fig. 5h**

Fig. 5h	
Table Analyzed	Correlation of TNF+GZMK+:GZMB+ and TU NFkB score
Column B	Log2 Ratio TNF+GZMK+:GZMB+ Exhausted
vs	vs
Column A	On Treatment TU NFkB/TNF score

Spearman Correlation	
P value	0.016
Exact or approximate P value?	exact
P value summary	*
Significantly different (P<0.05)?	Yes
rho value	0.59

997
998 **Fig. 5i**

Fig. 5i	
Table Analyzed	On Treatment TU NFkB/TNF Score
Column B	Group 1
vs	vs
Column A	Group 2
Wilcoxon Rank Sum Exact Test	
P value	0.031
Exact or approximate P value?	exact
P value summary	*
Significantly different (P<0.05)?	Yes
One- or two-tailed P value?	Two-tailed
W statistic	10
Lower 95% CI	-0.137790703
Upper 95% CI	-0.002177585

999
000 **Fig. 5j**

Table Analyzed	pre-ICI and pre-PD NLR
Column B	pre-PD
vs.	vs.
Column A	pre-ICI
Wilcoxon matched-pairs signed rank test	
P value	0.0195
Exact or approximate P value?	Exact
P value summary	*
Significantly different (P < 0.05)?	Yes
One- or two-tailed P value?	Two-tailed
Sum of positive, negative ranks	50.00 , -5.000
Sum of signed ranks (W)	45.00
Number of pairs	10
Number of ties (ignored)	0
Median of differences	
Median	1.329
How effective was the pairing?	
rs (Spearman)	0.8909
P value (one tailed)	0.0006
P value summary	***
Was the pairing significantly effective?	Yes

001
002 **Extended Data Fig. 5g**

Table Analyzed	coad MSS vs MSIH neutrophils

Column B	MSI-H
vs.	vs.
Column A	MSS
Mann Whitney test	
P value	0.0076
Exact or approximate P value?	Exact
P value summary	**
Significantly different (P < 0.05)?	Yes
One- or two-tailed P value?	Two-tailed
Sum of ranks in column A,B	13634 , 4132
Mann-Whitney U	2006
Difference between medians	
Median of column A	0.000, n=152
Median of column B	0.004083, n=36
Difference: Actual	0.004083
Difference: Hodges-Lehmann	0.001540

003